Project No. 11-3230

Enriched Boron-Doped Amorphous Selenium Based Position-Sensitive Solid-State Thermal Neutron Detector for MPACT Applications

Fuel Cycle Research and Development

Krishna Mandal
University of South Carolina

Dan Vega, Federal POC
Daneila Henzlova, Technical POC

NEUP Nuclear Energy University Programs
U.S. Department of Energy

Final Report

Project Title:	Enriched Boron-doped Amorphous Selenium based Position-Sensitive Solid-state Thermal Neutron Detector for MPACT Applications.
Date of Report:	September 29, 2017
Recipient:	University of South Carolina, Columbia, SC 29208
Award Number:	DE-AC07-05ID14517
Contract #:	120563
Principle Investigator:	Krishna C. Mandal, Tel. 803-777-2722, e-mail: mandalk@cec.sc.edu

Table of Content

1. Introduction

High-efficiency thermal neutron detectors with compact size, low power-rating and high spatial, temporal and energy resolution are essential to execute non-proliferation and safeguard protocols. The demands of such detector are not fully covered by the current detection system such as gas proportional counters or scintillator-photomultiplier tube combinations, which are limited by their detection efficiency, stability of response, speed of operation, and physical size. Furthermore, world-wide shortage of ^{3}He gas, required for widely used gas detection method, has further prompted to design an alternative system. Therefore, a solid-state neutron detection system without the requirement of ^{3}He will be very desirable.

To address the above technology gap, we had proposed to develop new room temperature solid-state thermal neutron detectors based on enriched boron (^{10}B) and enriched lithium (^{6}Li) doped amorphous Se (As- 0.52%, Cl 5 ppm) semiconductor for MPACT applications. The proposed alloy materials have been identified for its many favorable characteristics - a wide bandgap (~2.2 eV at 300 K) for room temperature operation, high glass transition temperature (t_g ~85°C), a high thermal neutron cross-section (for boron ~ 3840 barns, for lithium ~ 940 barns, 1 barn = 10^{-24} cm^2), low effective atomic number of Se for small gamma ray sensitivity, and high radiation tolerance due to its amorphous structure.

The ^{10}B (n, α) ^{7}Li Reaction and Thermal Neutron Detection: The conceptual design of solid-state 'direct read-out' 10B-doped a-Se (As, Cl) based thermal neutron detector is shown Figure 1. The neutrons when captured by the ^{10}B nucleus, which has a large cross section for thermal neutrons (3840 barns), undergo an (n, α) reaction, producing two energetic charged particles.

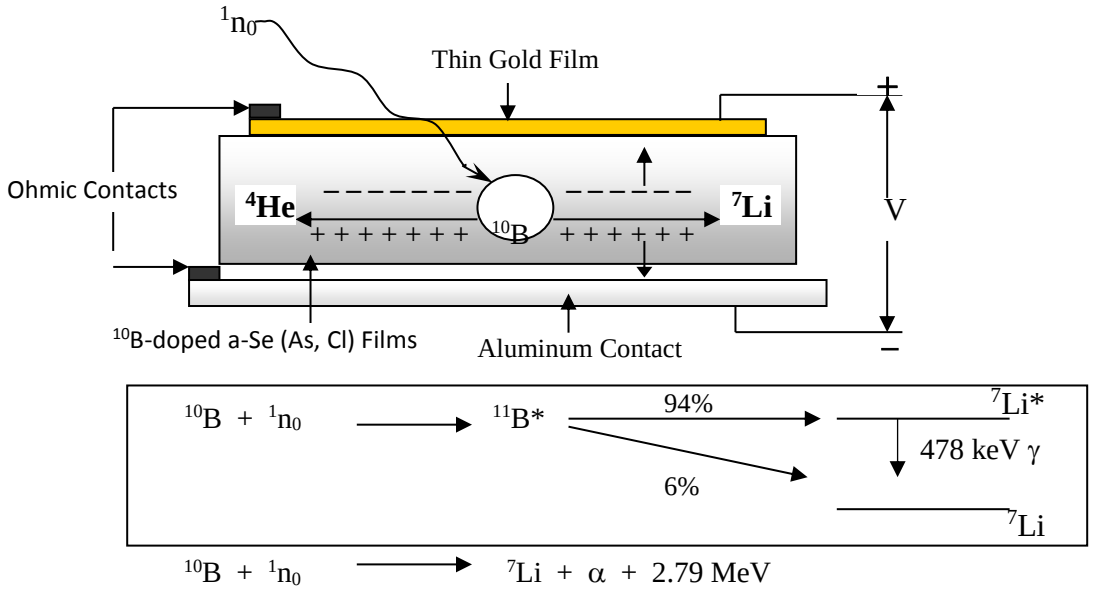

Figure 1. Conceptual design of a thermal neutron detector using B-doped a-Se (As, Cl) semiconductor films

The released 2.79 MeV kinetic energy is shared by the two charged particles traveling in opposite directions (energy of ^{7}Li = 1.014 MeV and E_{α} = 1.78 MeV). As with any charged particles of this energy, they have relatively short path lengths in solid materials and would be readily stopped, depositing their kinetic energy. The kinetic energy of the charged particles excites electrons into the lattice conduction band and displaces atoms from their lattice sites. The electrons excited into the conduction band (and holes in the valence band) are free to move and can produce a measurable electrical current upon application of an electric field across the a-Se film. The resulting signal pulse indicates the occurrence of a thermal neutron capture event. Standard nuclear-pulse type, charge-sensitive amplifier electronics are used to measure the current pulses.

A better neutron performance may be achieved with lithium (^{6}Li) doping since it has ~7 times longer range of the reaction products (t 32 - µm, ^{4}He 7 - µm) in Se compared to ^{10}B reaction products (α 4.2 - µm, ^{7}Li 2.1 - µm). Although ^{6}Li has lower thermal neutron cross section, the energies for ^{6}Li reaction products are much higher than that of ^{10}B, thereby, allowing for easier discrimination of background radiations. The spectral features for 6Li reaction products have a natural low energy valley, thereby, allowing for easy allocation of the lower level discriminator. The salient "wall effect" with 10B does not allow for this important advantage. In principle it could outperform ^{10}B provided similar concentrations can be achieved.

2. Organization of the Report

The research work plan and milestones identified for the project are listed in Section 3 of this report. In Section 4, major achievements are summarized, while description of work and results obtained for each tasks are detailed in Section 5. In Section 6 students involved in the project are listed, followed by resulting publications and presentations in Section 7.

3. Project Objective and Milestones

The objective of the project was to develop pathways for a room temperature direct readout solid-state thermal neutron detector based on enriched boron (^{10}B) (and also ^{6}Li) doped a-Se (As, Cl) alloy semiconductor. When fully developed, these detectors are expected to find widespread use in nuclear power plant including safeguard of special nuclear materials, reactor instrumentation, process monitoring, and nuclear waste management. The block diagram below depicts the research path followed in the program; the technical milestones identified for the project are listed thereafter.

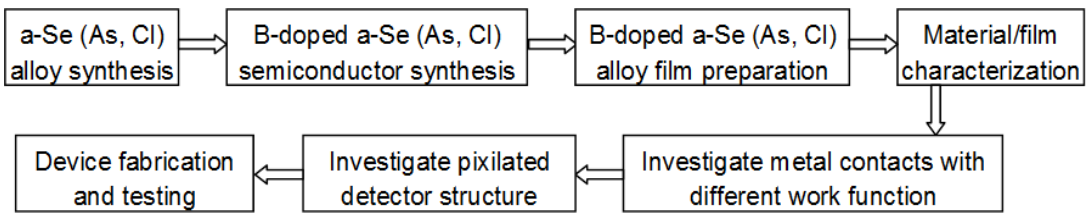

Milestone 1 - Demonstrate the feasibility of ^{10}B-doped a-Se alloys as potential direct read-out solid-state neutron detector.

Milestone 2 – Spectroscopic characterization of alloy material and detector films to determine morphology, opto-electronic, and charge transport properties in order to increase detector size and sensitivity.

Milestone 3 - Produce uniform alloy films up to 10 x 10 cm^2 area and 500 μm in thickness using enriched ^{10}B and ^{6}Li-doped a-Se (As, Cl) bulk alloys with up to 38 a/o enriched boron concentration.

Milestone 4 - Demonstrate nuclear radiation response using large-area (10 x 10 cm^2) detector based on ^{10}B-and ^{6}Li-doped a-Se (As, Cl) alloy thin films on various substrates including oxidized aluminum and ITO coated glass substrates

4. Major Accomplishments

In this research and development project following major goals were achieved.

- Feasibility of a new thermal neutron detector based on heavily ^{10}B-doped a-Se semiconductor film (5 x 5 cm^2 and 300 μm thick) was demonstrated. Alpha particles were employed as a surrogate for neutrons at this initial stage because of the comparative radiological ease of use of small alpha sources and the fact that the ^{10}B neutron capture reaction directly produces an alpha particle. (*Milestone 1*)

- Monodispersed boronated (^{10}B-doped a-Se) and lithiated (^{6}Li-doped a-Se) alloy materials were synthesized (~32 a/o), doping concentration using successively increased doping concentration in multiple master alloy synthetic steps. We have prepared several batches of different concentrated B/Li-doped alloys of monodispersed boron in a-Se (As,Cl) alloy matrix to increase the activity coefficient of boron in B-Se system or lithium in Li-Se system. By repeated alloy synthesis, we have avoided segregation of boron atomic species (formation of B_2Se_3) or lithium atomic species (precipitations of Li, or Li_2Se) within the dispersed alloy materials.

- Scanning electron microscopy (SEM) and x-ray photon spectroscopy (XPS) showed the films were defect free, X-ray diffraction (XRD) study confirmed the amorphous nature of the film, and Differential scanning calorimetry (DSC) confirmed the glass transition temperature and melting point. Infrared transmission spectroscopy (FTIR) was carried out to confirm any inclusions/precipitates of elemental boron or lithium across the thickness of the films detectors. A few large area films (10 × 10 cm^2) showed occasional polycrystallinity and inclusions/precipitates with low resistivity, especially when thickness approaching to 500 μm. (*Milestone 2*)

- The induced polycrystallinity issue was mitigated by changing the heat flux distribution of the substrate holder. We have addressed this issue with changing the design of substrate holder heating elements within the high vacuum chamber of our thermal evaporator. We have also tried slow deposition rate and low ramp-down cooling rate. We have also initiated the modeling of the heating elements through installing and calibrating multi-physics COMSOL program.

- A series of film deposition experiments and subsequent physical, optical, spectroscopic, and electrical characterization have been carried out to identify optimum deposition process to produce uniform and highly resistive (>10^{12} Ω-cm) alloy films up to 10 x 10 cm^2 area and >500 μm in thickness.
- Alloy films of 10 × 10 cm^2 with a thickness of ~525 μm were deposited using 32 a/o B-doped a-Se (0.52% As, 5 ppm Cl) alloy materials on prefabricated oxidized aluminum (Al_2O_3/Al) and on ITO coated glass substrates. We have achieved success of depositing up to ~550 μm lithiated a-Se alloy films without any induced polycrystallinity that showed very high resistivity and very low leakage currents. We have tried to increase boron concentration in a-Se (B, As, Cl)] bulk alloy materials to 38 a/o. However we have faced difficulties with boron segregation and formation of boron- or lithium-selenide compound (B_2Se_3, Li_2Se_3 etc.) within mono-dispersed alloy materials. This may be due to inherent solid solubility of boron or lithium within the alloy liquid melt. (*Milestone 3*)
- Contact studies were carried out using different metals (Au, Ni, W, In, Sn, Cu, Mo and Pd) with various work functions. Ni, Pd, W contacts show lowest leakage currents (~10^{-11}A at -800V). Current-voltage characteristic showed the dark current is <1 nA at high biases (forward and reverse) up to about ± 900V because of the fabricated detectors were completely amorphous keeping very high resistivity (>10^{12} Ω-cm). The bias stability was also established.
- Device with Al/Al_2O_3 layer as an electron blocking layer and/or Sb_2S_3 as a hole-blocking layer reduced the leakage current further of the device and improved performance by controlling carrier transport.
- Electronic noise analysis was carried out with front-end readout electronics to determine the impact of the electronic noise on the aggregate detector performance. The various noise contributions such as shot noise of the FET, leakage current in the detector, and thermal noise in the feedback resistor, are analyzed in terms of equivalent noise charge (ENC). Pulse-height spectra (PHS) were collected at each shaping time using a precision pulser at a set frequency and amplitude. A variation of the ENC as a function of shaping time for the charge sensitive preamplifier was determined.
- Installed charge mode and current mode (I-DLTS) experiments to characterize imperfections, point defects, and localized polycrystallinity. Due to very high resistivity of the amorphous detectors (both boronated and lithiated), we could not perform capacitance mode DLTS (C-DLTS) experiments. The I-DLTS spectra look very good because of achieving improved front-end readout electronics. The detector exhibiting the lowest leakage current was selected for the study based on the current limitation of the preamplifier used in the front-end readout electronics.
- Finally, Single and multi-element 10×10 cm^2 detectors were tested for neutron responses using moderated ^{252}Cf, ^{241}Am-Be, and ^{239}Pu-Be sources with varying gains, shaping times, and bias voltages. The clearly showed α-particles (^{241}Am, a surrogate of neutron) and thermal neutron response (^{252}Cf and Pu-Be sources with moderator and thermal neutron convertor). (*Milestone 4*)

5. Description of Tasks and Results

There were five major technical tasks identified to achieve the milestones established for the project. The work carried out and results obtained for each tasks are discussed below.

Task 1 - Amorphous-Se (0.52% As, 5 ppm Cl) Semiconductor Material Synthesis

Amorphous selenium (a-Se) was alloyed with arsenic and chlorine to improve physical and optoelectronic properties of a-Se. Alloying with arsenic (As) has been found to be very effective in retarding the a-Se crystallization rate. During our effort to make a-Se (As, Cl) alloys, we have found that a-Se with As content of ~0.52% is totally resistant to crystallization. A very small amount of Cl (~ 5 ppm) compensates the effect of As on the charge transport characteristics. Chlorine drastically increases the lifetime of holes (τ_h), while it decreases that of electrons (τ_e). Careful control of the alloy composition is therefore instrumental in ensuring detector performance.

The electrical properties of semiconductors strongly depend on the distributions of impurities which could produce a non-uniform electrical response across the detector which can seriously limit the device performance. Therefore commercially available selenium (Se) was further purified using an in-house computer-controlled, horizontal, multi-pass zone refining (ZR) system which redistributed the impurities resulting purer material presented in Figure 2. The impurity analysis of the zone-refined selenium material samples were analyzed using glow discharge mass spectrometry (GDMS). The relative error associated with the GDMS technique is reported to be about 20%. Table 1 summarizes the results of purification by zone-refining process, which clearly reduced several dopant impurities in commercially bought Se precursor. This zone-refined Se material was then used to make Se-alloys.

Figure 2. Zone refined a-Se ingots.

Table 1. Impurity analysis of zone-refined Se by GDMS showing reduction in elemental impurity (dopant) concentration after zone-purification.

Element	Concentration before ZR	Concentration after ZR
Se	Major	Major
Hg	6-8 ppm	<4 ppb
Pb	16 ppm	<6 ppb
Sn	12 ppb	Not Detected
Ag	4-6 ppm	Not Detected
Cu	25 ppm	0.2 ppm
Fe	10 ppm	Not Detected
Mg	6 ppm	Not Detected
Si	4-6 ppm	0.4 ppm
Te	6-8 ppm	0.35 ppm
H_2O	10-12 ppm	Not Detected

High quality a-Se (As, Cl) material synthesis have been conducted using a specially designed alloying reactor shown in Figure 3. In-house zone refined (ZR) Se material (≥7-nine) and commercially available high purity As (≥6-nine) were used for the synthesis. We first synthesized Se-As and Se-Cl master alloys which were then used to synthesize Se-As-Cl alloys. The alloy-processing synthesis route was conducted in a tightly argon-controlled glove box. A typical digital picture of the synthesized a-Se (As, Cl) alloy shots is presented in Figure 4.

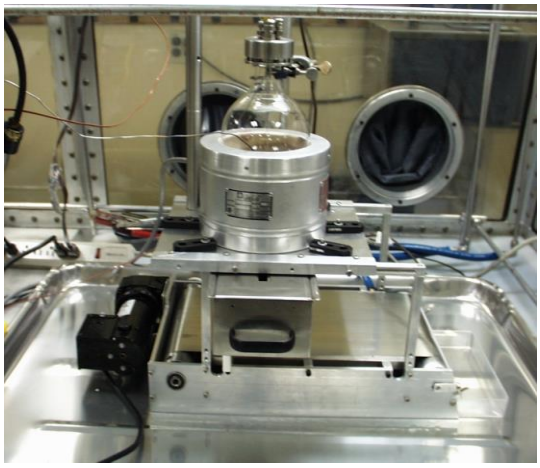

Figure 3. Installed a-Se (As, Cl) alloy reactor setup.

Figure 4. a-Se (As, Cl) alloy dry pellets.

Amorphous selenium alloy (a-Se) samples 0727G, 0727O, 0727R and 0727Y were synthesized at the University of South Carolina (USC) and characterized with Raman spectroscopy, differential

scanning calorimetry (DSC) and energy dispersive x-ray spectroscopy (EDS) at Fisk University, our collaborator. Figure 5 shows room temperature Raman spectra of a-Se alloy samples. Raman spectroscopy demonstrated that the samples 0727O and 0727R were in metastable monoclinic Se_8 states, in which seven vibrational modes located at 40(41), 59(60), 77, 110, 133, 227(228) and 251(252) cm^{-1} were found. The sample 0727G was in stable form of trigonal structure of Se_8, in which two modes at 142 and 234 cm^{-1} were found. Both Raman and EDS exhibited that a small amount of tellurium (Te) existed in 0727Y sample. DSC measurements were performed in TA Q200 system. DSC curves of the four samples (Figure 6) were significantly different. Samples 0727G and 0727O have one melting point, located at 219.6 and 98.7°C respectively. Samples of 0727R and 0727Y both possess two melting points, located at 50.0 and 215.3, and 56.6 and 225.3°C respectively. The surface morphology and microstructure of the synthesized alloys were thoroughly examined by SEM studies and a typical SEM picture is presented in Figure 7. The morphology clearly showed very smooth and shiny surfaces without any micro cracks or any other defects.

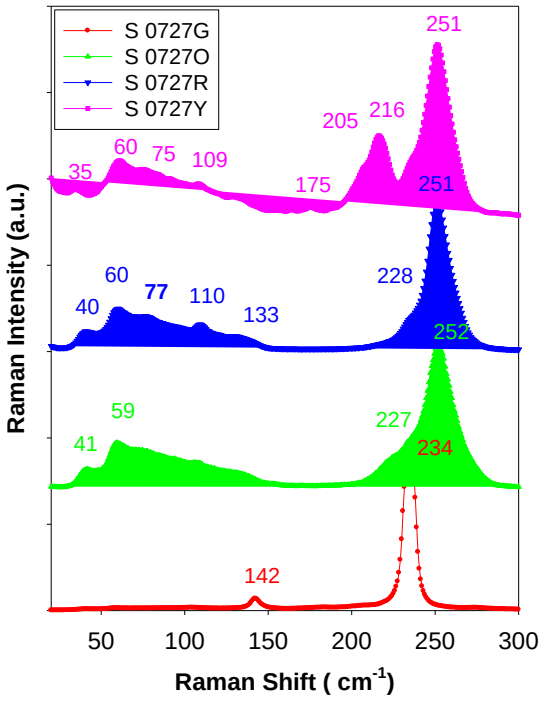

Figure 5. Room temperature Raman spectra of a-Se samples excited with 784-nm laser with a power density of 1 W/cm^2.

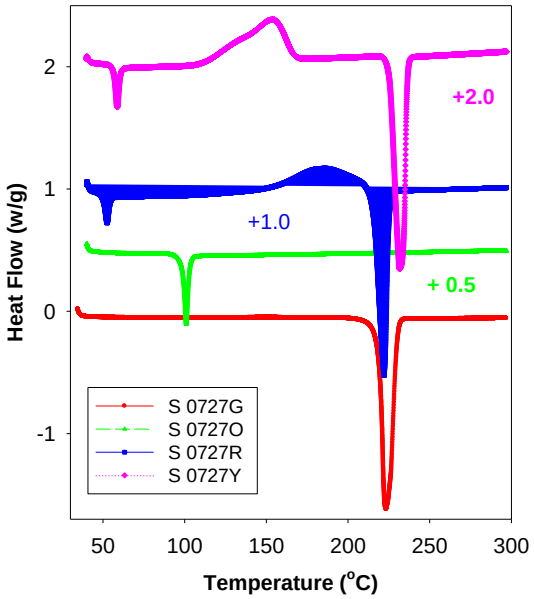

Figure 6. DSC curves of a-Se alloy samples. The heating rate was 10°C/min.

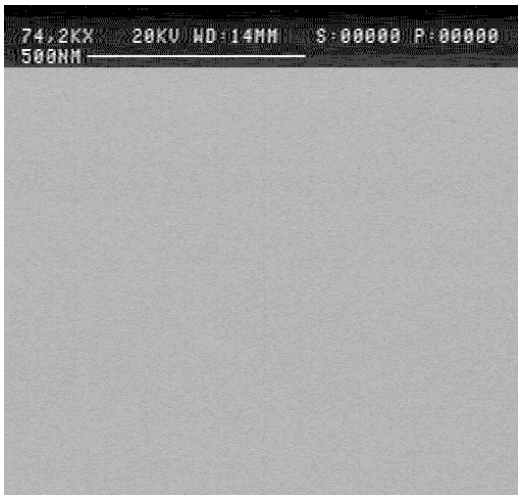

Figure 7. A typical SEM picture of a B-doped a-Se (As, Cl) alloy.

Task 2.1 - Synthesis of Boron- and Lithium-Doped a-Se (As, Cl) Alloy Material

The phase diagram of the B-Se system presented in Figure 8 shows that the thermodynamics of B alloy formation has major challenges associated with: 1) an immiscibility-gap on the selenium rich side, 2) formation of B_2Se_3 which is very stable and has a very low vapor pressure, and 3) the activity coefficient of B in the B-Se system is very low and so is the partial pressure of boron. The phase diagram of Li-Se system as presented in Figure 9 shows that the thermodynamics of Li-Se alloy formation also have similar problems as described for B-Se system. We have overcome these problems by heat treating the alloy melt at an elevated temperature for a short period of time (475^{o}C for 15 min. in case of B-doped alloy and 975^{o}C for 5 min. in case of Li-doped alloy) and preparing up to six alloys with different concentrations of mono-dispersed boron/lithium in a-Se (As, Cl) matrix to increase the activity coefficient of the active dopant. The key was to avoid the reaction of boron (or lithium) and selenium and successively increase doping concentrations in pre-synthesized alloys.

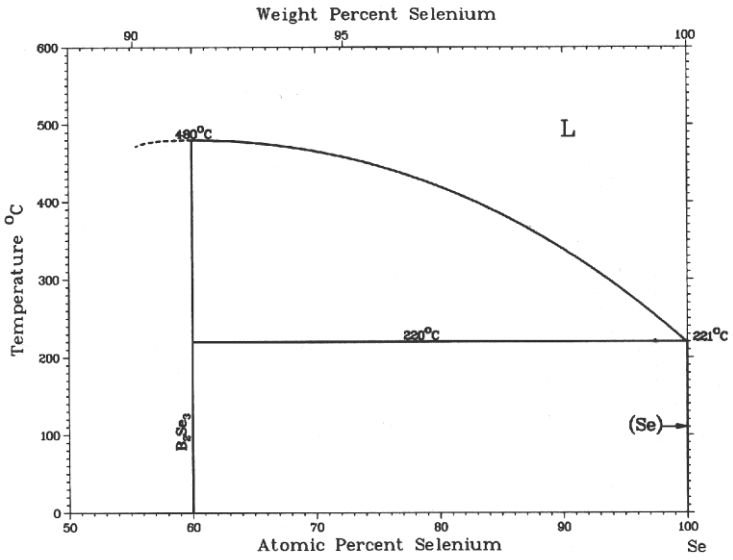

Figure 8. The phase diagram of B-Se system.

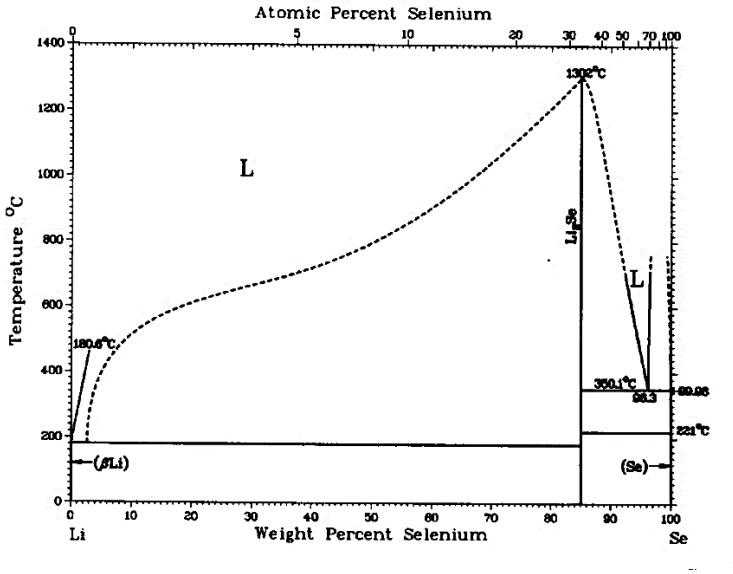

Figure 9. The Phase diagram of Li-Se system

Boron and lithium-doped a-Se (As, Cl) alloy materials were prepared using a special palletizing apparatus designed and constructed at USC. The process cycle was operated in a glove box maintained in a pure argon atmosphere. The alloy reactor was heated in a controlled manner using Omega PID temperature controller to 465°C for 5 hours and homogenized by a rotating impeller (50 - 100 rpm) to grow B-Se alloy. The reactor temperature was controlled at 500°C for Li-Se alloy. The melt was cooled to 355°C and shotting was performed with SS 316 shotter maintained at 360°C on a shotter plate at 6°C. Typical temperature profiles with alloying time for one process run is presented in Figure 10 for a-Se (B, As, Cl) alloy and in Figure 11 for a-Se (Li, As, Cl) alloy. Boron- and lithium-doped a-Se (As, Cl) alloy materials of with up to 32 a/o of enriched boron was synthesized. Figure 12 shows typical appearance of the synthesized boron-doped a-Se (As, Cl) alloy shots. The synthesized Li-Se alloy has similar dark color with shiny surface on one side.

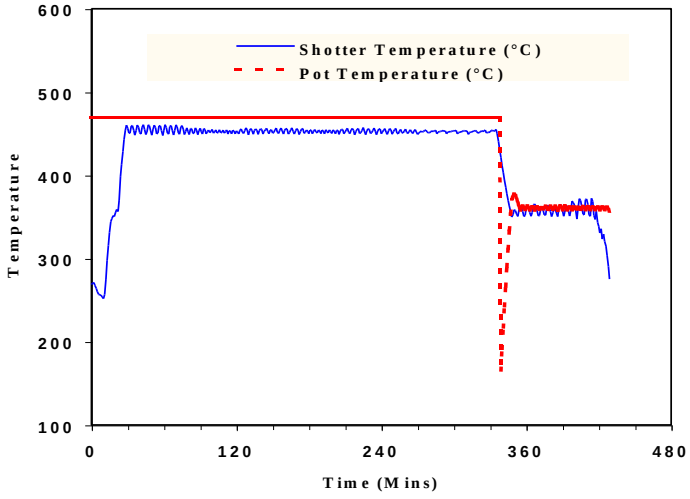

Figure 10. Temperature vs. time characteristics for B-doped a-Se (As, Cl) bulk alloy synthesis.

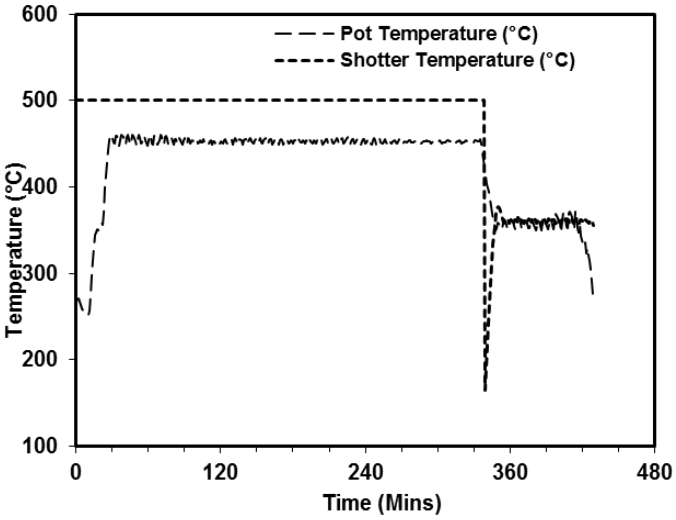

Figure 11. Temperature vs. Time characteristics for Li-doped a-Se (As, Cl) bulk alloy synthesis.

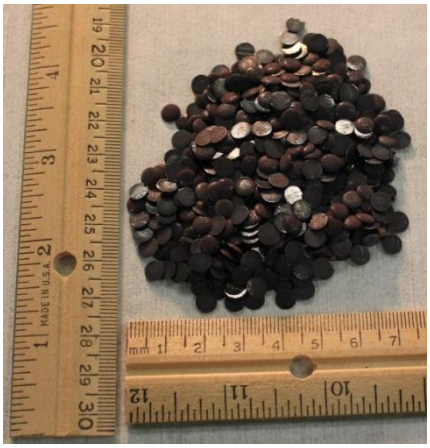

Figure 12. Dry pellets of ^{10}B-doped (32 a/o) a-Se (0.52%As, 5ppm Cl) alloy material.

Task 2.2 - Characterization of Boron- and Lithium-Doped a-Se (As, Cl) Alloy Material

X-ray Diffraction (XRD) was used to confirm the amorphous structure of selenium alloys. Typical XRD patterns of a-Se (As, Cl) alloys with or without boron-doping are shown in Figure 13. XRD patterns confirmed the amorphous structure of the alloys. No other peaks due to impurities or any other phases were observed within the sensitivity of the instrument (0.1%). Selenium has very high resistivity in amorphous phase, thus it is crucial to keep the amorphous structure. The shapes of the XRD patterns didn't change noticeably for different boron concentrations. No additional peaks appeared for different boron concentrations. The XRD results confirm that the material syntheses procedures were well controlled to form amorphous structures.

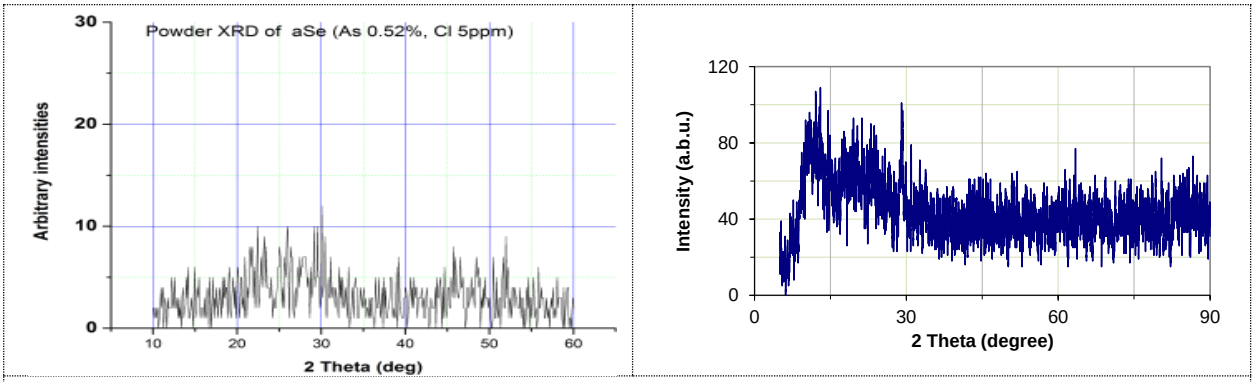

Figure 13. X-ray diffraction patterns showing amorphous structure: (Left) a-Se (As 0.52%, Cl 5 ppm) alloy and (Right) 32 a/o Boron-doped a-Se (As 0.52%, Cl 5 ppm) alloy.

X-ray photoelectrons spectroscopy (XPS) survey scans were carried out to examine B (or Li), As, and Cl concentrations at the surfaces as well as within its bulk. The XPS experiments were conducted using a Vacuum Generator ESCALAB MKII equipped with XPS/Auger spectrometer with a MgK$_\alpha$ source (E=1253.6 eV) with 300 W power at 15 KV. The XPS data in Figure 14 showed that there were no binding energy shifts, which explains clearly the absence of any compound (e.g., B_2Se_3 or B_2SeO_4) formations. Argon ion etching (5.0 KV; rate of sputtering 48 nm/min for Se) also confirmed the uniform distribution of alloying elements (B, As & Cl) from the surface towards the bulk depth up to 0.15 μm.

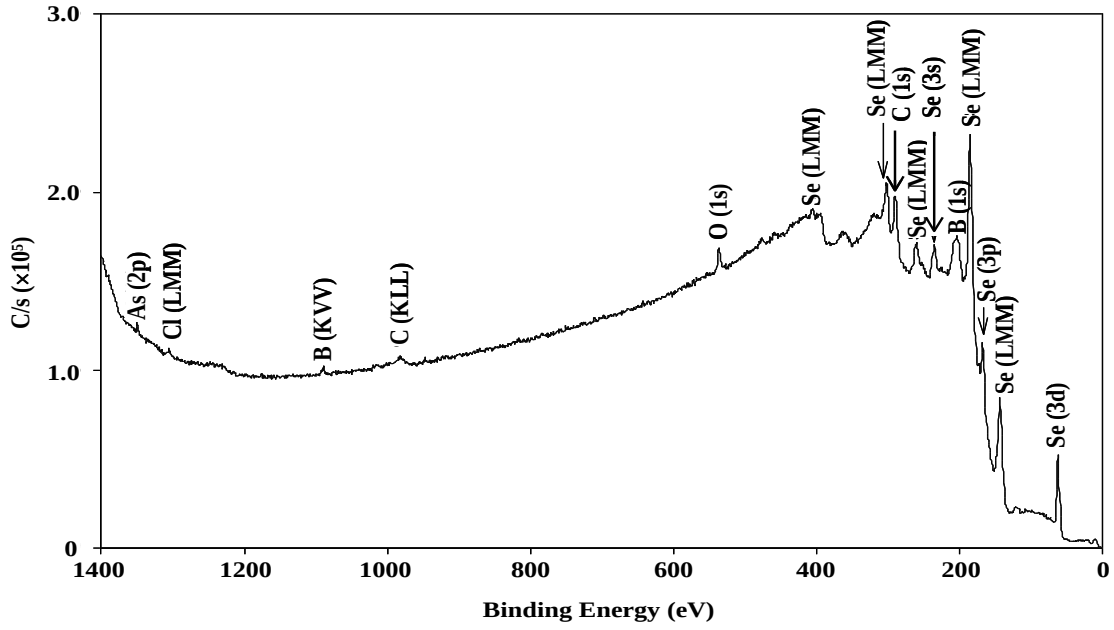

Figure 14. XPS survey scan on a B-doped a-Se (As, Cl) alloy material.

Fourier transformation infra-red (FTIR) measurements were taken to investigate structural effects of boron doping. The FTIR measurements were done by Nicolet 750 FTIR spectrometer. Figure

15 shows the IR transmission of Se (B, As, Cl) alloy with different B concentration. The vibration bands from the spectra are summarized in the Table 2. From the infrared transmission study, five major vibration bands appeared at wavenumber 750, 800, 859, 993, and 1250 cm^{-1} were identified with incorporation of boron. Some vibration bands matched the available reference values. However, due to limited references, more studies are needed to identify nature of all vibration bands.

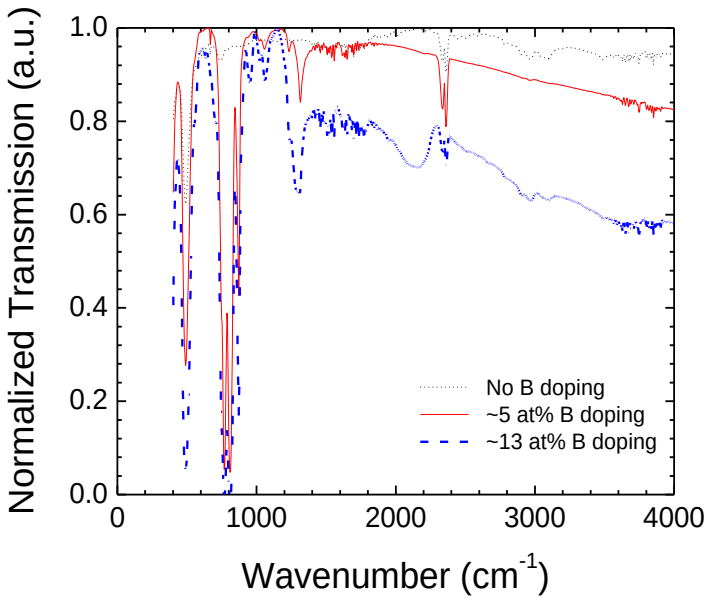

Figure 15. Fourier transformation infrared spectra on a-Se (B, As, Cl) alloy plate.

Table 2 Summary of observed vibration bands observed from the IR transmission spectra

Wavenumber (cm^{-1})	Possible identification	Effects on increased doping
487	Related to Se_8 rings	Increased slightly with increased boron doping
750 859	Related to Boron doping; possibly Se-B bonding	Most Distinct band appeared as boron was added and magnitude of the these peaks increased with increasing boron concentrations
993, 1032, 1043	Related to oxygen which exists in ambient	Does not show clear trend as boron concentration changes
1250	Might be attributed to B-B network	Remains similar at different doping
2350	Possibly due to CO_2 in ambient during measurement.	The band exists before boron doping and no correlation with boron concentration

Transmission two-modulator generalized ellipsometry (2-MGE) measurements were carried out for B-doped a-Se alloy samples. For 2-MGE measurements, wavelength selection was determined by the available light source, the optical elements in the path, the sample, filters used to select the wavelength, and the photodetector. A GaAs photomultiplier tube in conjunction with a mercury-xenon lamp was used and a band-pass filter was set at 890 nm, well below the band edge of B-doped a-Se alloys. Focusing was done as in a standard microscope, but with the emphasis on maximum light transmission rather than uniform field illumination, as in Kohler illumination. The objective was to have a large depth of focus. For B-doped a-Se alloy sample, a resolution of ~10-20 μm was obtained. In addition to this, the instrument determined the diattenuation, retardation, direction of the principal axis, circular diattenuation, and depolarization of the sample. Data were taken serially, pixel-by-pixel. B-doped a-Se alloy samples were characterized by scanning a 3 mm × 3 mm portion of sample with a pixel size of 20 μm.

The ellipsometry mapping pictures of boron-doped a-Se(As, Cl) alloy samples are shown in Figure 16. The intensity pictures (black and white picture in Figure 16a) shows dark spots that are typically 20-50 μm in diameters and are probably different phases in the Se material due to boron inclusions. The values of diattenuation (Figure 16b), depolarization (Figure 16d), and retardation (Figure 16e) showed some variation over the 3 mm × 3 mm sample size (compare area at the right side of the sample to the left side or middle of the sample). Changes in direction of the principal axis were also observed from region to region. Thus spectroscopic ellipsometry measurements show B doped a-Se alloy samples are slightly phase separated.

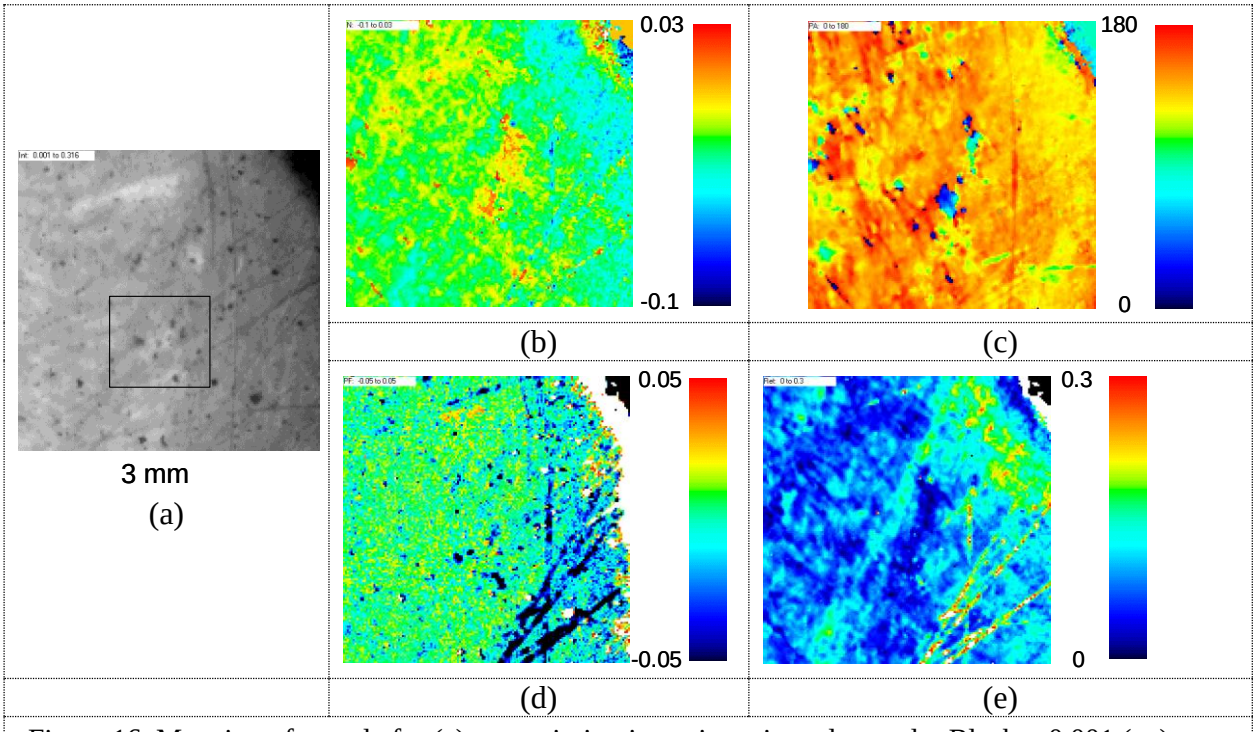

Figure 16. Mapping of sample for (a) transmission intensity using a log scale- Black = 0.001 (au), White = 0.316 (au), (b) diattenuation, (c) direction of the principal axis. (d) depolarization, and (e) retardation. (λ = 890 nm and pixel size = 20 μm)

Task 3.1 – Deposition of Boron- and Lithium-doped a-Se (As, Cl) Films

Thin film deposition was carried out using thermal evaporation system as shown in Figure 17 – a CHA SE 600 evaporator equipped with planetary rotation system under high vacuum (base pressure $2x10^{-6}$ Torr). Vacuum fixtures, in-situ quartz crystal monitoring head, and substrate temperature accessories were installed within the thermal evaporation system. At a pressure of 2 x 10^{-6} torr the substrates were heated to 68ºC ± 0.5ºC by an automatic thermostat system, comprised of electrical resistive heaters. The evaporation source was temperature controlled as well. The source was preheated to 280ºC at a rate of about 15ºC/min, then kept it at 280ºC for 2 min., while the evaporation rate stabilized to ~3.5 μm per minute. The source temperature was then adjusted to keep the rate constant within 5%. The substrate was shuttered during the heating ramp, rate stabilization, and post-deposition cool-down steps to avoid contamination. Samples were allowed to cool-down to 30ºC before being removed from the evaporator.

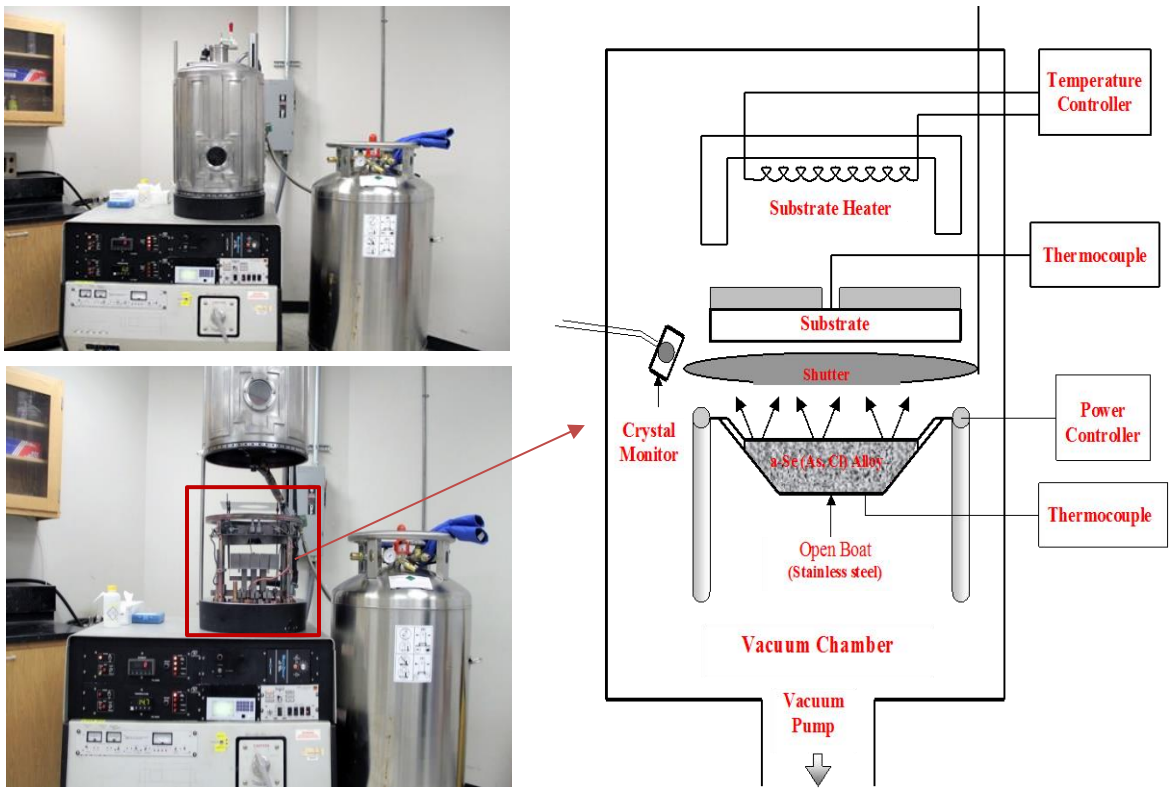

Figure 17. Thin film evaporation system used to deposit B/Li-doped a-Se (As, Cl) alloy films – (left) .pictures of the system and (right) schematic diagram.

It was necessary to grow the films with completely amorphous phase in order to obtain very high resistivity. The boron- or lithium-doped amorphous selenium alloys have poor thermal conductivity and have lower transition temperature than conventional semiconductors. Therefore to avoid polycrystallization, the substrate temperature was constantly monitored during the deposition process so that the temperature of the film does not reach above its crystallization temperature. If the substrate temperature reached around 10°C below the transition temperature, the film was cooled down by turning off the power to the evaporation source. Then, the deposition

was resumed when the substrate was sufficiently cooled down. Film thicknesses were measured by Dektak IIA surface profilometer and the depositions were monitored by a quartz crystal thickness monitor.

The films were grown on the various size substrates (oxidized aluminum and ITO coated glass) with the largest area of 10 x 10 cm^2 (4″ × 4″). Aluminum substrates with 1/8" thickness and ITO substrates with 0.5 mm were pre-cleaned successively with acetone, isopropanol and DI water and were dried by immersing into an ultrasonic vapor degreaser. Aluminum substrate etching was conducted in a caustic solution of sodium phosphate carbonate solution (for 3 min), and then dipped in concentrated nitric acid (for 2 min). The substrates were finally rinsed thoroughly with DI water. Then substrates were dried under constant flow of N_2 gas. Then, the substrates were oxidized in a furnace by heating them at 350°C for 3 hours in air. After etching and oxidation, the surface of the Al substrates became whitish instead of a dark gray color. This substrate preparation step is critical because poorly prepared substrates result in large leakage currents.

Using the procedures above, we have successfully produced smooth, surface-defect free thicker layers of B-doped a-Se (As, Cl) alloy films (525 μm thick) on ITO coated glass (up to 2 x 2 sq. inches = 25cm^2) and oxidized aluminum substrates (up to 4 x 4 sq. inches = 100 cm^2). Pictures of some of the deposited films are shown in Figure 18 and Figure 19. Figure 20 shows the films deposited in a single run.

Thicker films preparation involved longer hours (≥ 10 hours) taking into consideration full pumping-up, baking interior fixtures, substrate heating & stabilizing, and final pumping-down with slow cooling rate. Therefore in films with a thickness of ~ 500 μm, it was difficult to preserve complete amorphous structure during long run time because of induced strain with higher thickness caused by induced crystallization (poly-crystallinity).

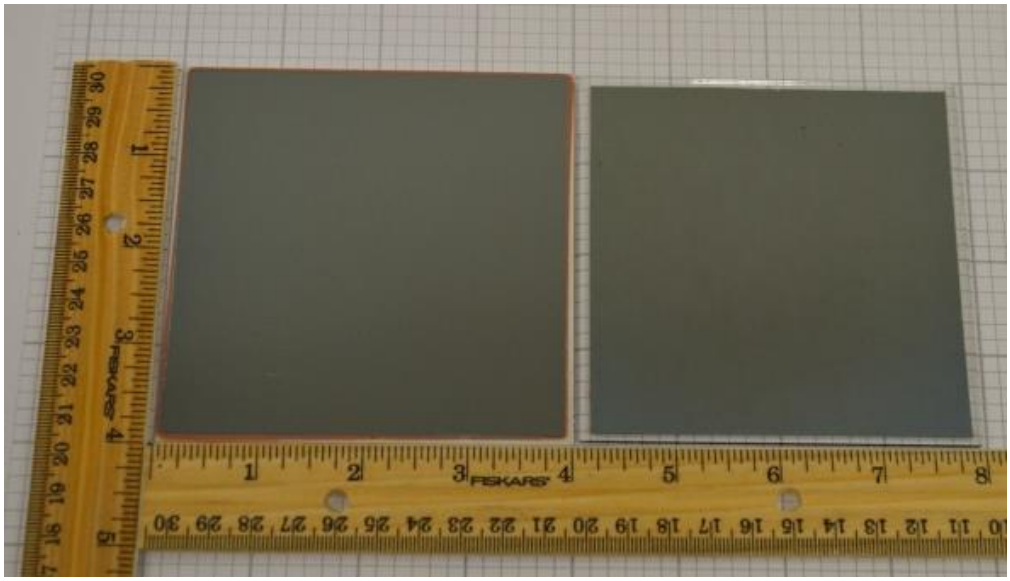

Figure 18. Enriched ^{10}B-doped a-Se (As, Cl) thin films with ~450 μm thickness deposited on 10 x 10 cm^2 (4x4 sq. inches) substrates: (left) Al/Al_2O_3 substrate and (right) ITO coated glass substrate.

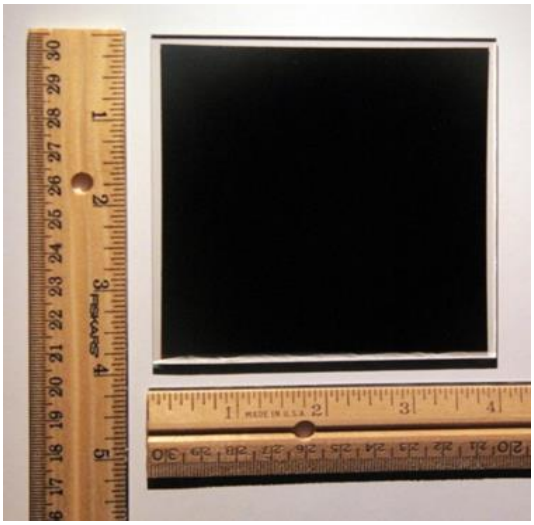

Figure 19. Lithium-doped a-Se alloy films (525 μm thickness) on 10 x 10 cm^2 (4x4 sq. inches) ITO coated glass substrates.

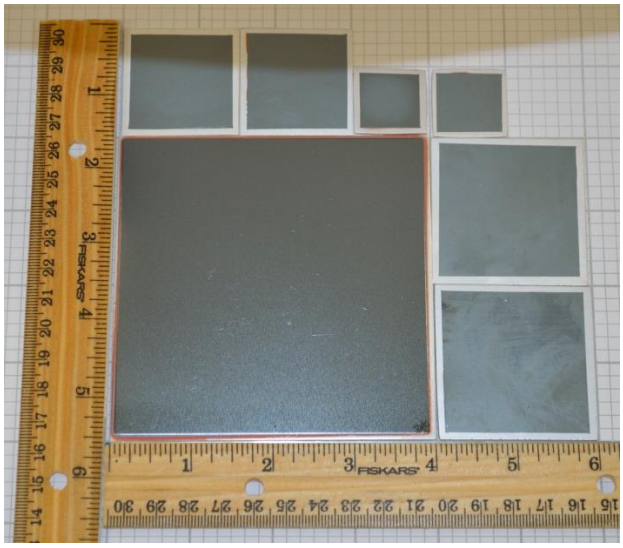

Figure 20. Various sizes of boron-doped a-Se (As, Cl) thin films on Al/Al_2O_3 substrates deposited in a single deposition run.

Task 3.2 – Characterization of Boron- and Lithium-doped a-Se (As, Cl) Films

Scanning electron microscopy (SEM) was used for surface morphology characterization of the deposited films. The appearances of typical high-quality 32 a/o B-doped a-Se alloy films are presented in Figure 21. The SEM pictures showed smooth surfaces without any micro-cracks, devoid of any induced polycrystallinity or major defects. A few large area films (10×10 cm^2) showed occasional polycrystallinity and inclusions/precipitates with low resistivity, especially when thickness approaching to ≥500 μm (see Figure 22).

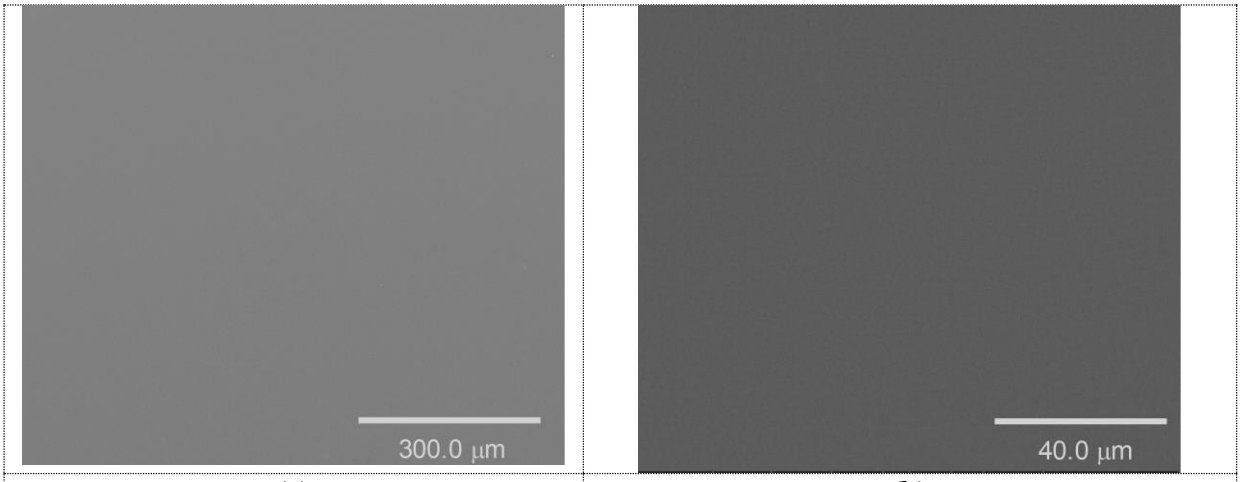

(a) (b)

Figure 21. SEM pictures of 32 a/o B-doped a-Se (As, Cl) thin films (400 μm) on (a) ITO coated glass substrate and (b) oxidized aluminum substrate.

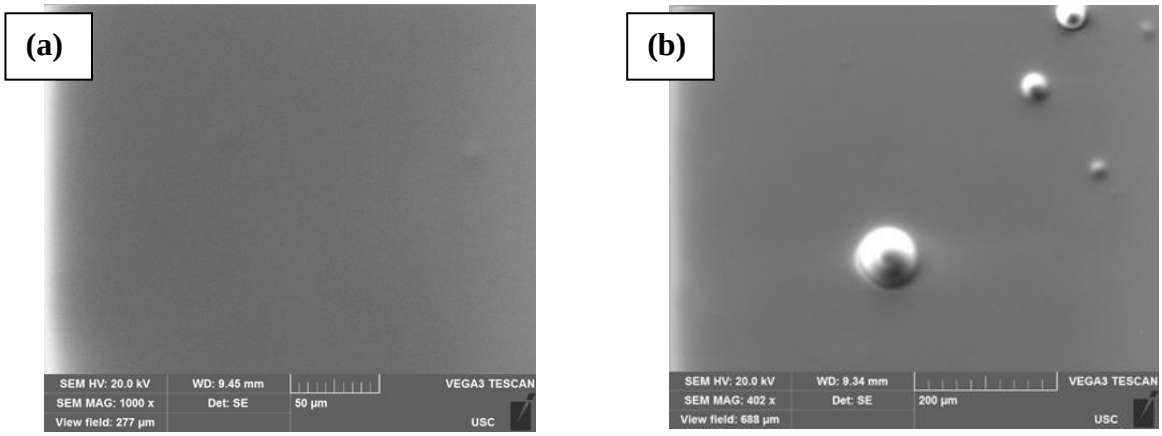

Figure 22. (a) SEM images of 450 µm Li-doped a-Se (As, Cl) alloy film on ITO-glass substrate showing smooth surface; (b) magnified image showing a few surface defects.

Cross sectional morphology and uniformity of element concentration was investigated using SEM/EDAX measurements (Figure 23). The counts of Cl are very small because the concentration is in ppm level, boron is not observed because of low atomic mass. For boron concentration, ICP-MS and GDMS were performed.

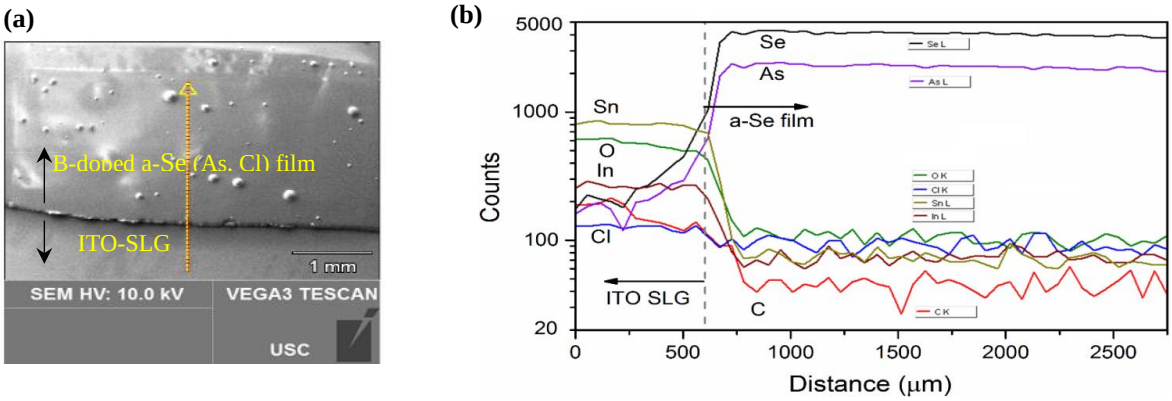

(c)

Alloys	Elements	Concentration
a-Se-B-As-Cl	**Se**	**Major**
	B	**32.4 ± 0.8 a/o**
	As	**0.51± 0.04%**
	Cl	**5 ± 2 ppm**

Figure 23. (a) SEM image taken at the edge of the B-doped a-Se (As, Cl) alloy film on ITO-coated glass substrates; (b) EDAX line scan showing the elemental concentration along the yellow arrow shown in 'a'; (c) GDMS analysis of boron-doped a-Se (As, Cl) alloy.

X-ray Diffraction (XRD) analysis was used to confirm the amorphous structure of 32 a/o B/Li-doped selenium alloy film. The observed diffraction pattern shown in Figure 24 corresponded very well to the standard x-ray pattern for Se alloys with an amorphous structure. There are no diffraction peaks identifiable for any major or minor crystallographic orientation. No other peaks due to impurities or any other phases were observed within the sensitivity of the instrument (0.1%).

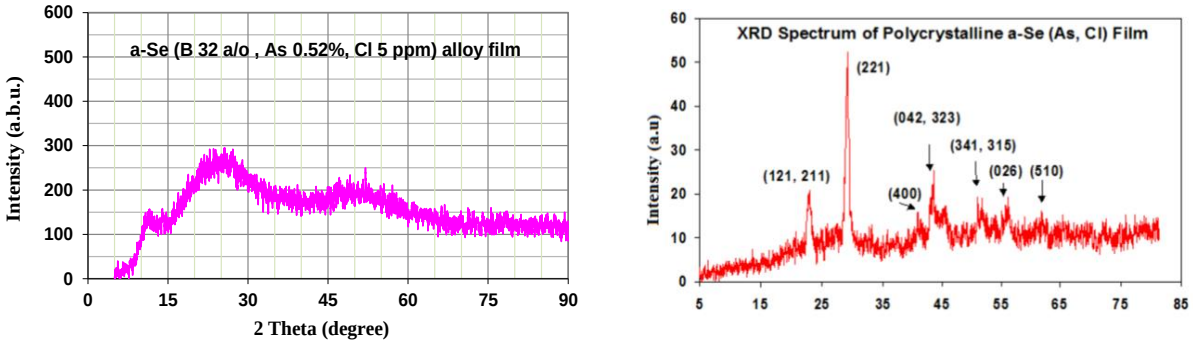

Figure 24. XRD patterns: (left) amorphous structure of 32 a/o boron-doped a-Se (As, Cl) alloy film and (right) a polycrystalline a-Se (As, Cl) alloy film for comparison.

Differential scanning calorimetry (DSC) measurements were carried out to determine the glass transition temperatures, crystalline temperatures, and melting temperatures of the boron-doped alloys. The sample was loaded into a gold-coated stainless steel pan and hermetically sealed. An empty pan was used as a reference. The sample was first cooled from room temperature of 25°C to 0°C at a rate 10°C/min and stabilized at 0°C for two minutes. Then, it was heated at the same rate (10°C/min) to about 275°C, well above the melting temperature. The cell was then stabilized for two minutes and then the cooling scans were initiated at a rate of 10°C/min to 0°C and then brought back to 25°C. The glass transition temperatures, crystalline temperatures, and melting temperatures measured during heating and cooling cycles were clearly identified and measured to be 59.9°C, 132.9°C, and 221.8°C, respectively for 32a/o boron-doped a-Se(As, Cl) alloy (Figure 25). The DSC result showed that the glass transition temperature and melting point of the alloy increased after boron doping compared to un-doped a-Se(As, Cl) alloy sample.

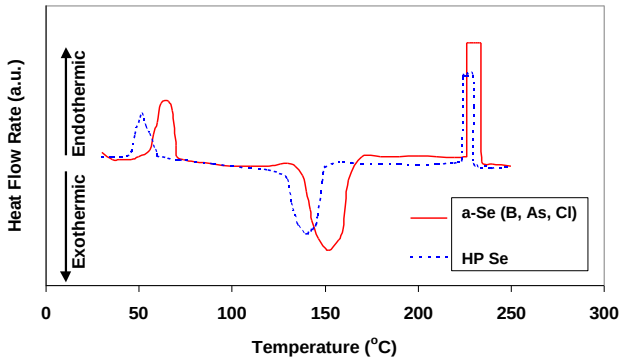

DSC results before and after boron-doping

	a-Se (As, Cl) alloy (0727R in Figure 6)	32% B-doped a-Se (As, Cl) alloy
Glass Transition Temperature	50.0°C	59.9°C
Melting Point	215.3°C	221.8°C

Figure 25. DSC traces of boron-doped a-Se (As, Cl) alloy sample at a scan rate of 10 °C/min. The table at right compares DSC data for alloy samples with or without boron doping.

X-ray photoemission (XPS) investigations of the a-Se (Li, As, Cl) alloys were carried out to examine Li, As, and Cl concentrations at the film surfaces as well as within its bulk. This experiment was conducted using a Vacuum Generator ESCALAB MKII equipped with XPS/Auger spectrometer with a MgK_{α} source (E=1253.6 eV) with 300 W power at 15 KV. Data acquisition and analysis for XPS used a Physical Electronics multiple technique analytical

computer system with Physical Electronics version 6 software. The work function of the spectrometer on the basis of the Au $4f_{3/2}$ peak energy of 83.8 eV and the reported binding energies here are referenced to C (1s) at 284.6 eV. All the binding energies quoted here are within ±0.3 eV. The survey scan and high-resolution energy peaks are presented in Figure 26, Figure 27, and Figure 28, respectively. The peak energies were measured after the data were smoothed. The observed binding energies of the Se 3d (53.9 eV), Li 1s (58.4 eV), As $3p_{3/2}$ (141.8 eV) and $3P_{1/2}$ (146.4 eV), and Cl 2p (198.4 eV) correspond very well with a-Se (Li, As, Cl) alloying elements. There are no binding energy shifts, which explains clearly the absence of any compound formations. Argon ion etching (5.0 KV; rate of sputtering 48 nm/min for Se) confirms also the uniform distribution of alloying elements (Li, As & Cl) from surface towards depth up to 0.18 μm.

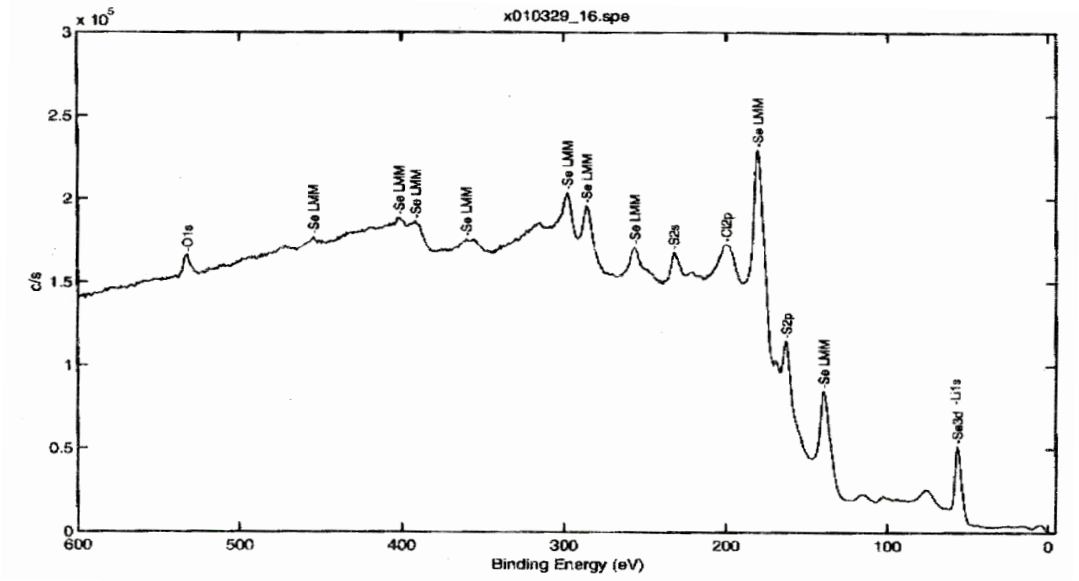

Figure 26. XPS survey scan for a-Se (Li, As, Cl) alloy film on ITO.

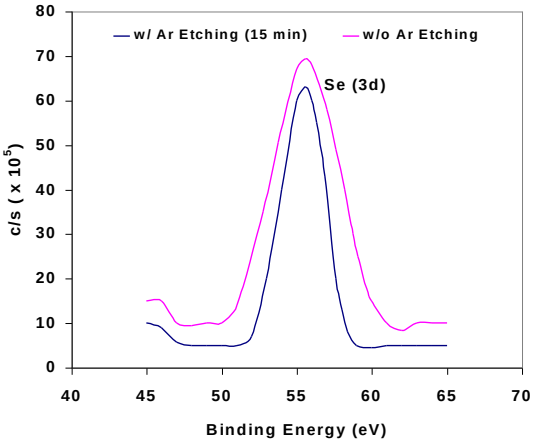

Figure 27. Spectra of Se (3d) level on a-Se (Li, As, Cl) alloy film with and without argon ion etching (15 minutes).

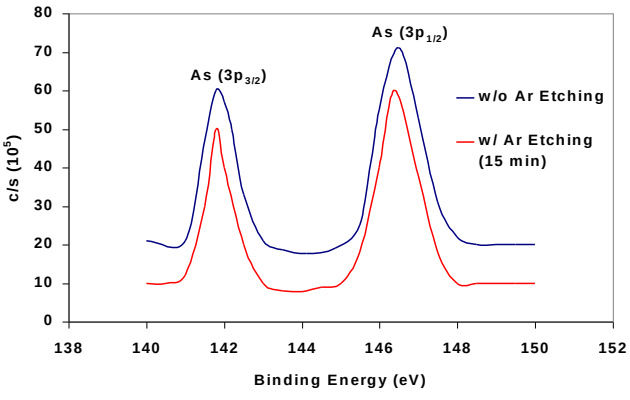

Figure 28. High-resolution XPS spectra of As ($3p_{1/2}$ $3p_{3/2}$) levels on a-Se (Li, As, Cl) alloy films with and without argon ion etching (15 minutes)

The optical absorption studies were conducted in order to confirm the energy bandgap of the alloying material. Figure 29 shows a typical optical absorption $(\alpha h\nu)^{1/2}$ vs. incident photon energy ($h\nu$, eV) curve. An identical ITO coated glass slide was used as the reference and the values of optical absorption coefficient (α) were not corrected for the reflection of the Li-doped a-Se alloy (As, Cl) surface. The energy bandgap (E_g) was estimated to be about 2.21 eV at 300K and in close agreement with other a-Se based alloys.

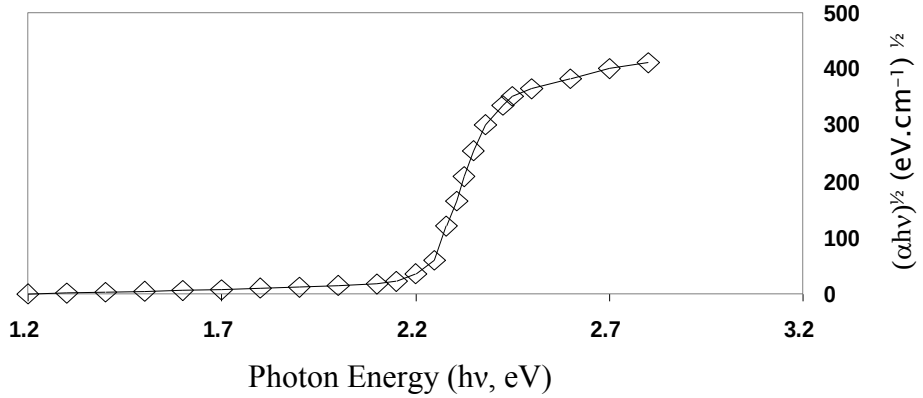

Figure 29. Optical absorption spectra on a-Se (Li, As, Cl) alloy film.

Task 4.1 - Detector Fabrication and Characterization

Using the deposited a-Se (^{10}B, As, Cl) films, devices with three different contact structures were studied to reduce the leakage current of the device by controlling carrier transport inside the devices for better detection signals. Similar structures were also used with Li-doped alloy films.

- Au /a-Se (^{10}B, As, Cl)/ Glass/ITO
- Au /a-Se (^{10}B, As, Cl)/ Al_2O_3/Al
- Au /Sb_2S_3 /a-Se (^{10}B, As, Cl)/ Al_2O_3/Al

Aluminum oxide (Al/Al_2O_3) layers was used as an electron blocking layer at the interface between the B-Se alloy and the substrate. The layer prevents dark current injection from the substrate and also aids the growth of uniform amorphous selenium layers. The aluminum oxide layer (120 nm) was deposited by evaporating 99.8 % Al_2O_3 (Cerac) in a Cu crucible with a deposition rate of 1.5-2.5 Å/s and a pressure of 2×10^{-6} Torr. The aluminum bottom contacts (150 nm) were then deposited by evaporating Al pellets (5N, purchased from Super Conductor Materials) in a BN crucible with a deposition rate of 1.5-2.5 Å/s and a base pressure of 2×10^{-6} Torr.

The top free surface of B-doped a-Se (As, Cl) layer normally acts as a blocking layer for holes preventing injection of surface charges into the bulk. However, an acceptor impurity such as chlorine has an opposite effect on charge injection. As the bias increases across the thickness of the film, electric field strength increases significantly at the air/Se-alloy interface (electrostatic discharge) enhancing charge carrier injection. A thin layer of antimony sulfide (Sb_2S_3) was thus also tested as a hole-blocking layer. Sb_2S_3 layer (560 nm) was deposited by evaporating 99.9 % Sb_2S_3 (purchased from Cerac) in an Al_2O_3 crucible with a deposition rate of ~10 Å/s with a base pressure of 2×10^{-6} Torr. Figure 30 shows the SEM pictures of Al_2O_3 and Sb_2S_3 films deposited for the electron and hole blocking layers, respectively.

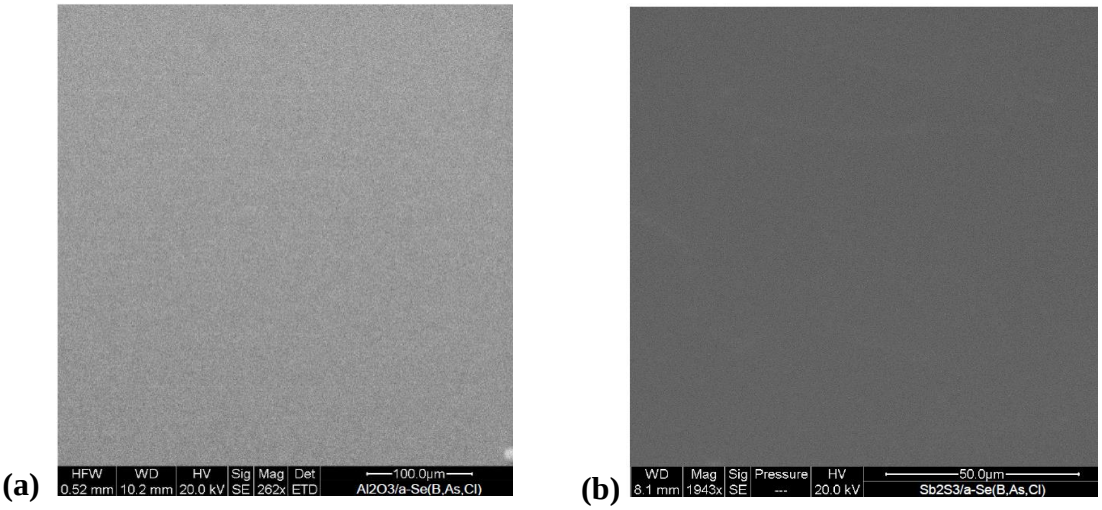

Figure 30. SEM pictures of (a) Al_2O_3 and (b) Sb_2S_3 films.

Metal contacts were deposited on the top and bottom surfaces of the alloy films by using metallization shadow mask techniques. The top contact was semitransparent gold of thickness 6-10 nm deposited by DC or radio frequency sputtering (RF). Thin copper wires were attached with silver epoxy and the contact area was encapsulated with very thin epoxy adhesives (surlyn (Dupont 1702) or standard glass frits). Pictures of a few of fabricated detectors are presented in Figure 31 and the facilities used to fabricate the detectors in Figure 32.

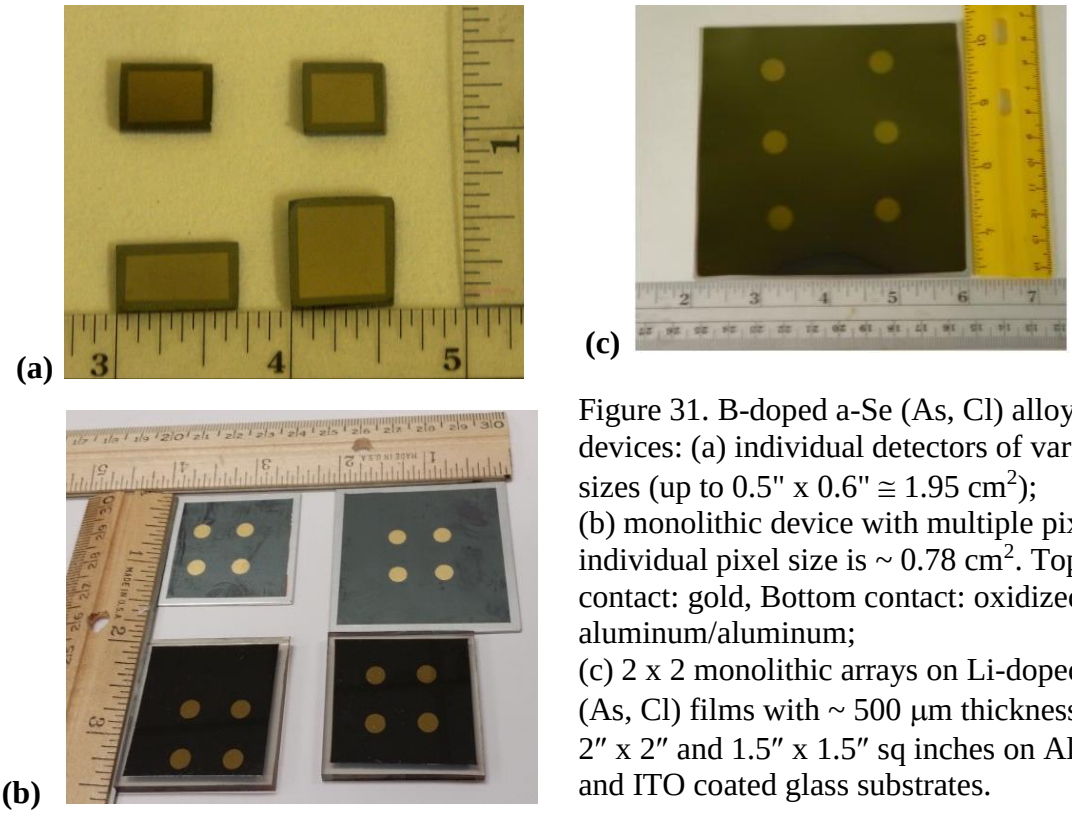

Figure 31. B-doped a-Se (As, Cl) alloy film devices: (a) individual detectors of various sizes (up to 0.5" x 0.6" ≅ 1.95 cm^2);
(b) monolithic device with multiple pixel; individual pixel size is ~ 0.78 cm^2. Top contact: gold, Bottom contact: oxidized aluminum/aluminum;
(c) 2 x 2 monolithic arrays on Li-doped a-Se (As, Cl) films with ~ 500 μm thickness on 2″ x 2″ and 1.5″ x 1.5″ sq inches on Al/Al_2O_3 and ITO coated glass substrates.

Clean room

Photolithography: Karl Suss model MJB 3 Mask Aligner, Min. pitch size: 0.5 μm

RF/DC 13.56 MHz frequency sputtering unit

Figure 32. Pictures of the facilities used to fabricate boron- and lithium-doped a-Se detectors.

Current-voltage (I-V) measurement were carried out by using Keithley 237 source measure unit and Metric ICS (version: 3.8.0) software. I-V measurements were recorded to determine detectors' resistivities and leakage currents by varying applied voltages. Figure 33 shows the current-voltage (I-V) characteristic of B-doped a-Se (As, Cl) alloy sample with top and bottom gold contacts. The result indicates low leakage current (~-10 nA at -1000V), and high rectification ratios showing typical diode characteristics. The low leakage current at a very high bias is beneficial for detector performance because higher electric field can be applied to the detector without increasing noise and that will enhance the signal from a detector. Results also showed high field penetration (i.e., strong charge carrier depletion) into the device and high field tolerance (up to 8 V/μm).

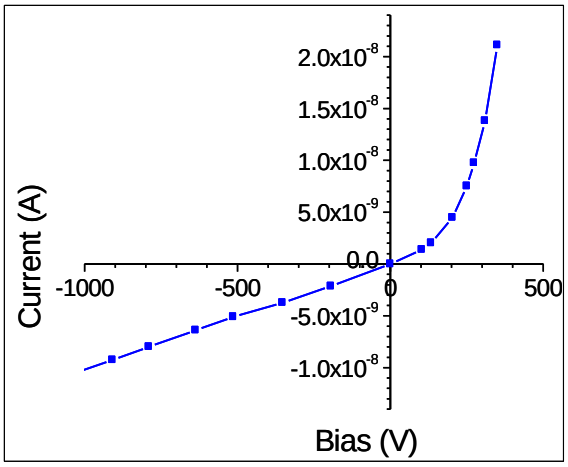

Figure 33. Current-voltage characteristics of an enriched ^{10}B-doped a-Se (B, As, Cl) detector without blocking layer.

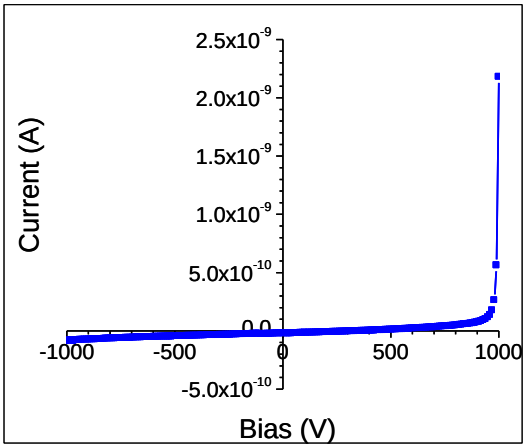

Figure 34. Current-voltage characteristics of an enriched ^{10}B-doped a-Se (B, As, Cl) detector with Al/Al_2O_3 electron blocking layer.

Figure 34 shows an I-V characteristic of an enriched ^{10}B-doped a-Se (B, As, Cl) detector with Al/Al_2O_3 as electron blocking layer. The resistivity measurements of the film devices showed the resistivity of ~10^{12} Ω·cm for the gold top electrode and the aluminum oxide and aluminum bottom

electrode devices. The devices with Al/Al_2O_3 electron blocking layer showed two to three orders of magnitude higher resistivity compared with the devices without an electron blocking layer. This is a promising result, which can further improve the performance of a-Se (B, As, Cl) alloy detectors by reducing leakage current significantly. The leakage current reduced further by adding a hole-blocking Sb_2S_3/Au layer and the resulting resistivity was in the range of 10^{13} Ω-cm.

Task 4.2 – Contact Studies

Contact studies were carried out to investigate the junction properties between B- or L-doped a-Se (As, Cl) and a wide variety of metals with different work functions (Au, Ni, W, Pd, Cu, Mo, In, and Sn). The aim was to investigate whether the choice of metal can improve the signal-to-noise ratio thereby performance of the detector by minimizing the dark leakage current. Metal deposition has been carried out by RF/DC 13.56 MHz frequency sputtering unit in argon ambient. Monolithic 3 x 3 arrays of metal contacts (M-S-M devices) for contact studies are presented in Figure 35. Current-voltage (I-V) characteristics of various metals are shown in Figure 36.

Metal	Work functions, ϕ_m (eV)	Metal	Work functions, ϕ_m (eV)
Au	5.1	Cu	4.65
Ni	5.15	Mo	4.37
Pd	5.12	In	4.12
W	4.55	Sn	4.42

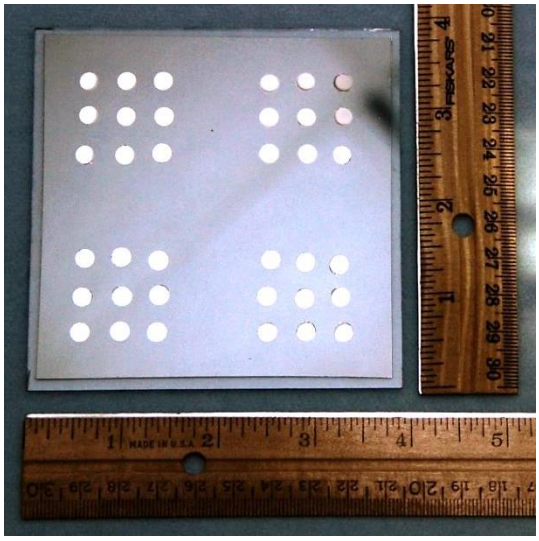

(a)

Upper left: gold (Au); upper right: nickel (Ni); lower left: Tungsten (W); and lower right: palladium (Pd)

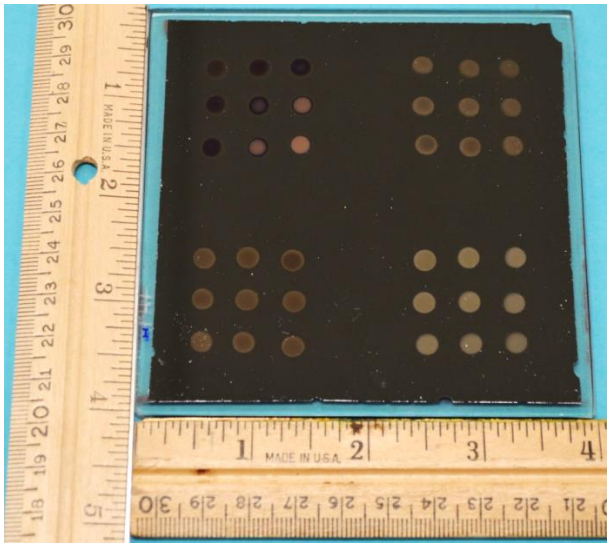

(b)

Upper left: copper (Cu); upper right: molybdenum (Mo); lower left: indium(In); and lower right: tin (Sn).

Figure 35. Metal contacts (monolithic 3 x 3 arrays) on 10×10 cm^2 (4 × 4 sq. inches) B-doped Se (As, Cl) thin film deposited on ITO-coated glass substrate.

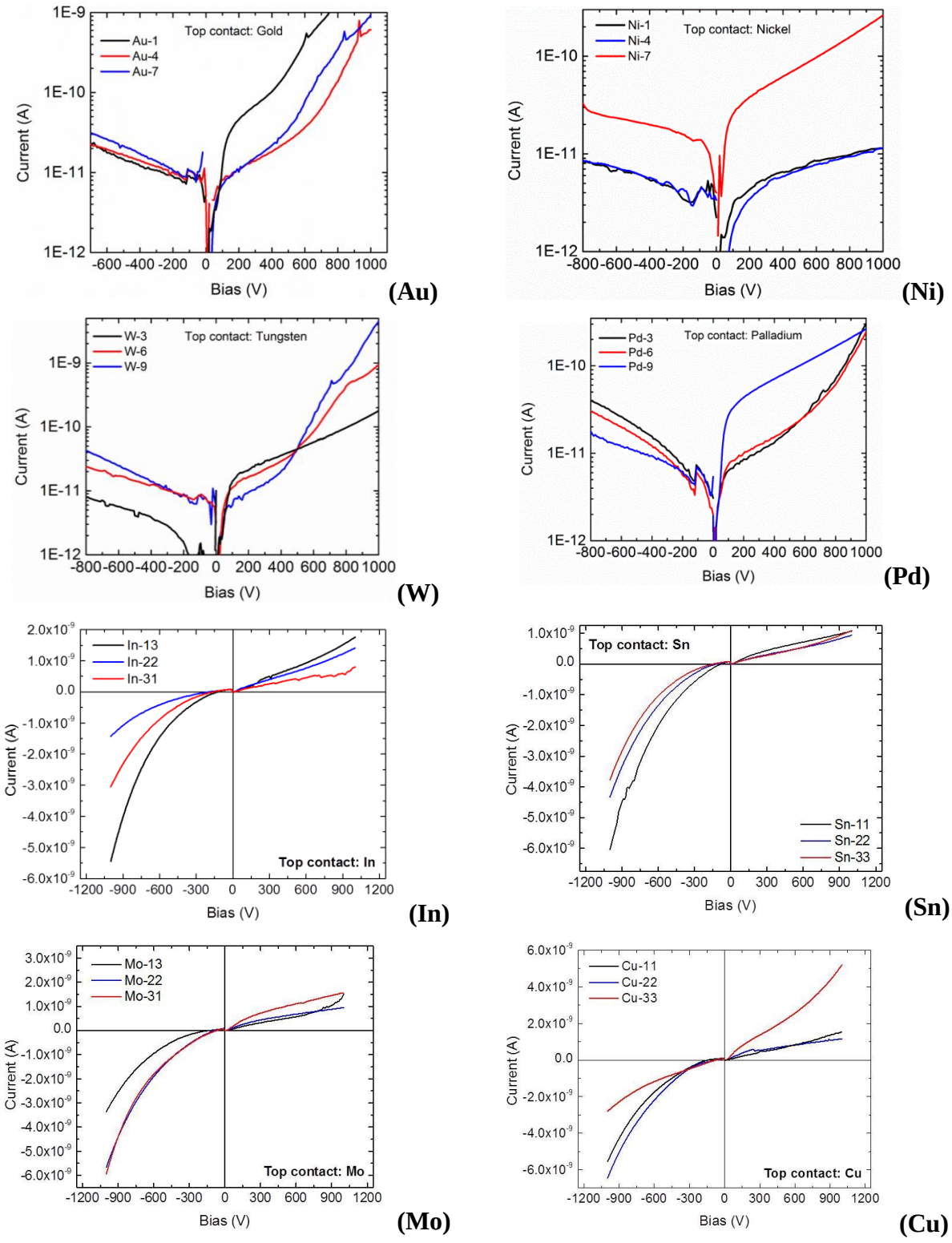

Figure 36. Current-voltage characteristics of various metals. I-V characteristics show very low leakage currents in the forward and reverse biases. The performance of Ni and W contacts show lowest leakage current (~ 10^{-11}A at -800V).

For the top metal contacts, we have found significant dependencies of metal work functions on current transients following application of voltages from -800 to 1000 volts. I-V characteristics show very low leakage currents in the forward and reverse biases. The performances of Ni and W contacts show lowest leakage currents (~ 10^{-11}A at -800V). Forward bias voltage degradations were observed for some contacts especially with Ni, Pd, Cu and Sn contacts. By evaluating the barrier height dependency on the metal work function, we were able to estimate the space charge densities by using time of flight (TOF) measurements. Capacitance-voltage (C-V) characteristics was measured on a-Se films with three selected Schottky barrier metals namely palladium (Pd), tungsten (W), and gold (Au). The C-V results show high Schottky barrier height (≥ 1.2 eV at 300K) and diode ideality factors between 1.1 and 1.3.

Figure 37 shows the current-voltage (I-V) characteristics of ^{6}Li-Se alloy detectors with four different 100 nm thick, circular, gold (Au) top contacts (identified as S 0-38, S 49-59, S 59-70, and S 70-80 respectively) to show their uniformities. The resistivities were found to be similar and in the range of 2 - 4 x 10^{11} Ω-cm at 1000 V bias. The overall spread of measured resistivity values is fairly narrow, meaning good reproducibility and uniformity of the fabricated detectors. The results also indicated low leakage currents (15-25 nA at 1000V).

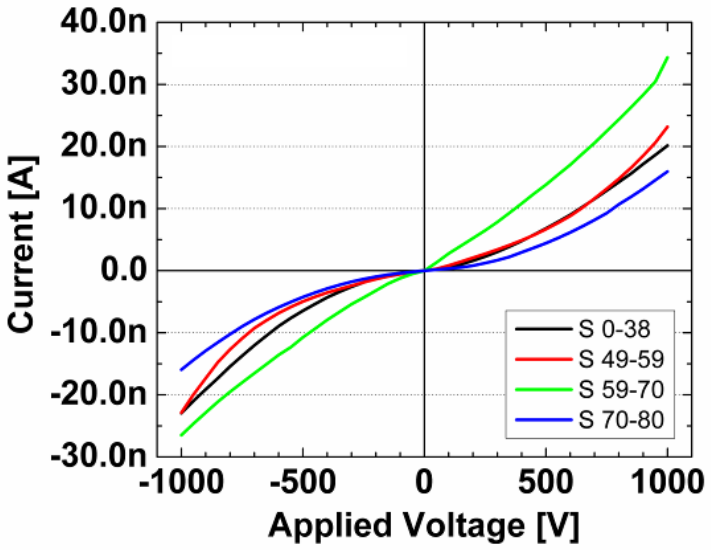

Figure 37. Current-voltage (I-V) characteristics of ^{6}Li-Se alloy detectors S 0-38, S 49-59, S 59-70, and S 70-80 respectively.

Task 5.1 –Calibration and Noise Analysis of the Nuclear Detection System

Before the detection system can give relevant information about the energy of detected radiation, it must be calibrated in terms of electronic noise performance. This is because the various parameters within a detection system, such as the gain of the preamplifier and shaping amplifier, the shaping time of the amplifier, and the noise present in the system, will contribute to changes in the pulse heights seen at the output of the shaping amplifier. In order to correlate the pulse height of a detection signal with its corresponding energy, calibration must be done under the same settings and similar configuration as the setup used to test a radiation detector.

System Calibration - Detailed energy calibration experiments in terms of electronic noise performance has been conducted in our new front-end read-out electronics system shown in Figure 38. The detection set up has been calibrated using a pulser, which generates waveforms and simulates the output of a radiation detector, is connected to the detection system through a capacitor. Pulses of fixed heights (V_{pulser}) are fed to the pre-amplifier signal input using a precision pulser through a feed through standard/calibrated capacitor (C_{test}) and pulse-height spectrum is acquired. Using Eqn. 1, the energy of the charge pulses from the capacitor, E_{pulser}, can be translated in terms of keV assuming that the pulses are generated in a particular semiconductor.

$$E_{pulser}(keV) = \frac{V_{pulser}(mV) \times W\left(\frac{eV}{ehp}\right) \times C_{test}(pF)}{1.6 \times 10^{-19}} \qquad \ldots Eqn\ (1)$$

where, W is the electron-hole pair creation energy. The corresponding pulser peak position in terms of channel number of the MCA is also noted. This step is repeated by changing the pulse height systematically. A graphical plot between the E_{pulser} and corresponding MCA peak position for different pulse heights gives the calibration graph. Figure 39(a) shows one MCA spectrum with various pulser peak-positions taken during calibration and Figure 39(b) is the corresponding calibration graph equivalent to a detector with a typical shaping amplifier and MCA settings. Using the calibration equation, values obtained in terms of MCA channel numbers are converted to energy units in keV.

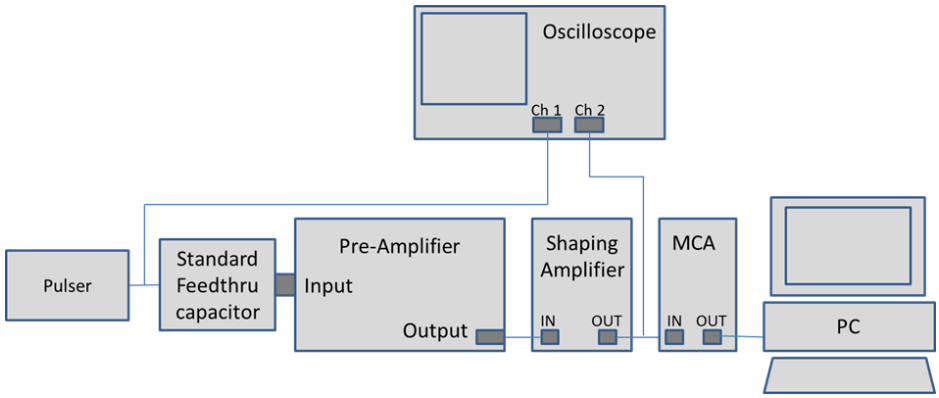

Figure 38. Schematic of a read-out electronics under calibration conditions.

(a)

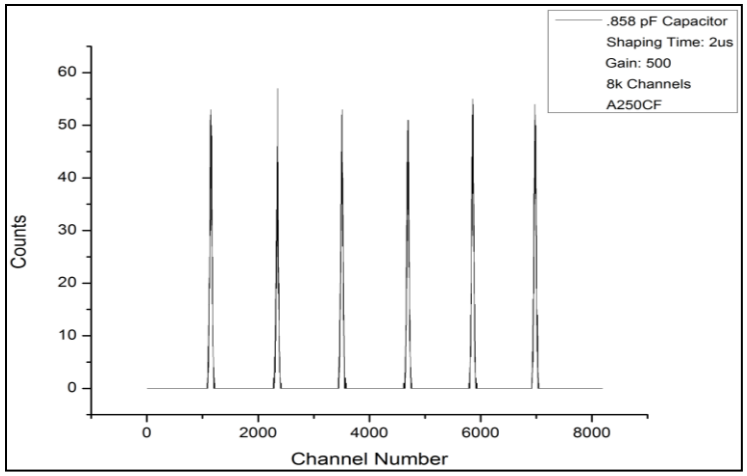

(b)

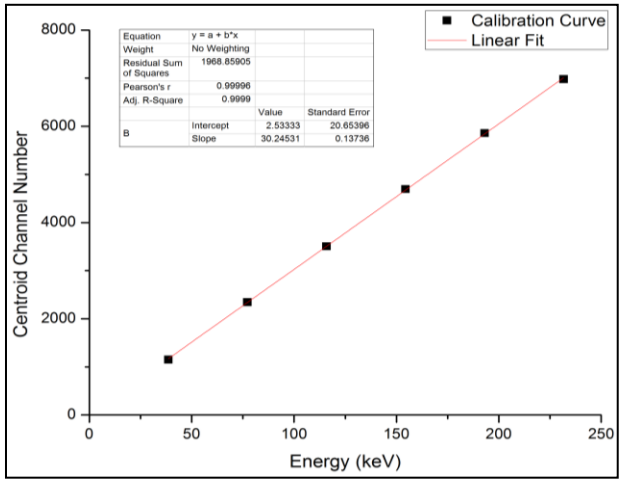

Figure 39. (a) Pulse height spectrum obtained for six different pulse sizes (b) calibration curve.

Noise measurements - In a radiation detection system, there are several sources of noise, which contribute to random fluctuations present in the detection signal. The ultimate performance of a nuclear detector is limited by the noise incurred by the associated electronics like the pre-amplifier, ADC, MCA etc. So it is very much necessary to know the magnitude of electronic noise involved. There are mainly three types of noise present which affect detection systems: thermal noise, shot noise, and flicker noise. Thermal noise appears approximately white, and therefore appears uniformly throughout the frequency spectrum. Shot noise is comprised of random statistical fluctuations in the electrical current of a DC circuit, due to the discrete nature of charge. The third type of electronic noise in detection systems is flicker noise, also known as 1/f noise. Flicker noise is caused by statistical resistance variations which play more of a role in lower frequency signals than in higher frequency signals. One source of flicker noise in front-end electronics is generation and recombination noise in a transistor due to base current.

The level of electronic noise in our set up has been determined using a precision pulser and a standard capacitor. Pulses of fixed amplitudes were fed to the input of the pre-amplifier through a calibrated feed-through capacitor and pulse-height spectrum was acquired using the desired amplifier and MCA settings. Noise is normally expressed in terms of the width (FWHM) of the pulser peak in the pulse height spectra.

We have adopted the formalism described by Bertuccio and Pullia in order to standardize our detection system in terms of optimized noise performance. The noise in a detection circuit is generally described by the equivalent noise charge (ENC). A least squared fitting algorithm based on the mathematical model of ENC was developed using MATLAB and applied to calculate the ENC of our detection system and the various components of the electronic noise.

The experimental values of *ENC* can be interpolated as a linear relationship for the squared equivalent noise charge as given in Eqn. 2.

$$ENC^2 = (aC_{tot}^2 A_1)\,{}^1\!/_\tau + \left[\left(2\pi a_f C_{tot}^2 + {}^{b_f}\!/_{2\pi}\right)A_2\right] + (bA_3)\tau = h_1 1/\tau + h_2 + h_3\tau \qquad Eqn\ (2)$$

where *A1*, *A2* and *A3* are constants depending on the shaping network response. C_{tot} is the total input capacitance, a_f is the coefficient of the FET noise, and b_f is the dielectric noise coefficient.

The white series contribution due to the thermal noise of the FET channel is expressed as *a*.

$$a = \alpha\frac{2KT}{g_m}, \qquad Eqn\ (3)$$

where g_m is the FET transconductance, α is a coefficient ranging from 0.5 to 0.7 depending on the FET working point.

The sum of the white parallel contribution (*b*) due to the shot noise of the FET and the detector leakage current I_L, and of the thermal noise of the feedback resistor R_f.is expressed as,

$$b = qI_L + \frac{2KT}{R_f} = qI_{eq}, \qquad Eqn\ (4)$$

Figure 40 shows the variation of ENC with a detector (biased and exposed to the alpha source) connected to the pre-amplifier. Various noise contributions were calculated as a function of different shaping times. It can be seen that the minimum ENC in the system when a detector is connected corresponds to a shaping time in between 3 and 6 μs.

In order to study the effect of detector capacitance and leakage current on the electronic noise, a bias dependent study of the electronic noise of the detection system was carried out. The ENCs have been measured at six different reverse bias voltages viz. -10, -30, -50, -70, -90, and -120 V. Figure 41 shows the variation of the ENC and the separate contributions to the electronic noise as a function of applied reverse bias for a shaping time of 3 μs. The increase in reverse bias reduces the detector junction capacitance and simultaneously increases the leakage current too. From the Figure 41 it can be noticed that the contribution of the white series noise dominated towards the overall noise and decreases with the increasing reverse bias or decreasing capacitance which is in consistence with Eqn. 2. The pink noise follows a similar trend which again is in agreement with Eqn. 2. The white parallel noise, which incorporates the detector leakage current, was seen to contribute the least at lower biases and increase steadily with reverse bias due to the increase in leakage current. It can also be noticed that beyond a reverse bias of -50 V, the contribution of the white parallel noise exceeded that of the pink noise.

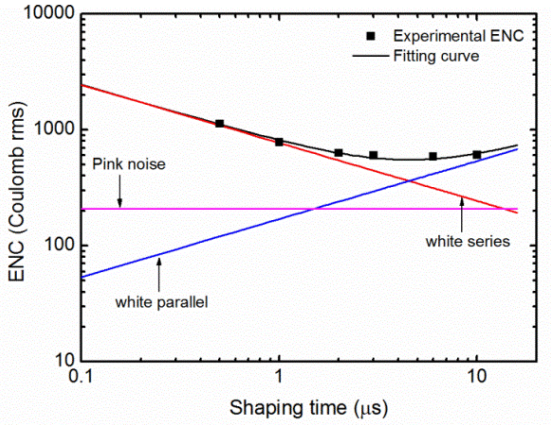

Figure 40. Variation of equivalent noise charge as a function of shaping time with a detector connected to the pre-amplifier. The detector was biased to -90 V and exposed to the ^{241}Am source during the measurements.

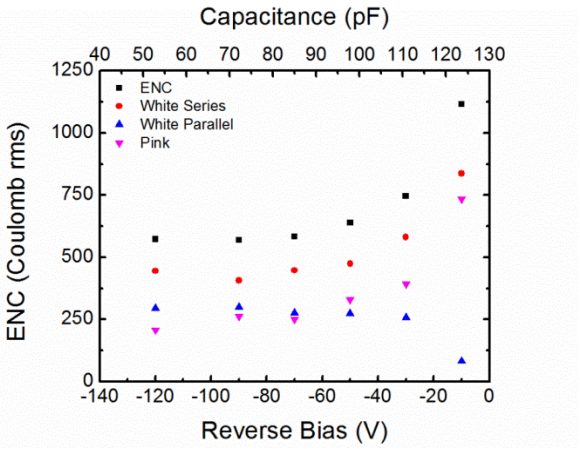

Figure 41. Variation of ENC, white series noise, pink noise and white parallel noise, measured using 3 μs shaping time, as a function of different bias voltages/detector capacitance.

Task 5.2 – Radiation Testing with Nuclear Radiation Sources

The response of the fabricated detectors to charged particles was first evaluated by irradiating the detector with α-particles (^{241}Am source). Alpha particles were employed as a surrogate for neutrons because of the comparative radiological ease of use of small alpha sources and the fact that the ^{10}B neutron capture reaction directly produces an alpha particle. The radiation spectrum was taken by using standard nuclear instrumentation consisting of a preamplifier, shaping amplifier and multi-channel analyzers (MCA). Figure 42 shows the schematic diagram of the detection testing setup. Figure 43 and Figure 44 show digital pictures of the detection testing setup and a detector testing stage.

The detectors front and back contacts were electrically connected to a charge sensitive preamplifier. The semitransparent Au contact was exposed to alpha particles. The response of the detectors to the nuclear particles was evaluated by irradiating the detector with an uncollimated 0.7 μCi ^{241}Am source (peak energies: 60 keV for γ and 5.5 MeV for α particles) and by recording the pulse height spectrum produced from the detector. The front contact was biased at -1000 volts. The bias to the detector was applied using a Canberra 3102D high voltage power supply. The charge signals generated by the interaction of the nuclear particles with the detector were amplified with a Princeton Gamma-Tech RG-11B/C-RT preamplifier, and a Canberra 2022 linear amplifier. The amplified signal was then fed into a Canberra Multiport II multichannel analyzer and evaluated using Genie-2000 software. The device was mounted on an insulating alumina plate onto a stud inside an EMI shielded aluminum box which was constantly evacuated using a rotary pump in order to minimize scattering of alpha-particle with air molecules.

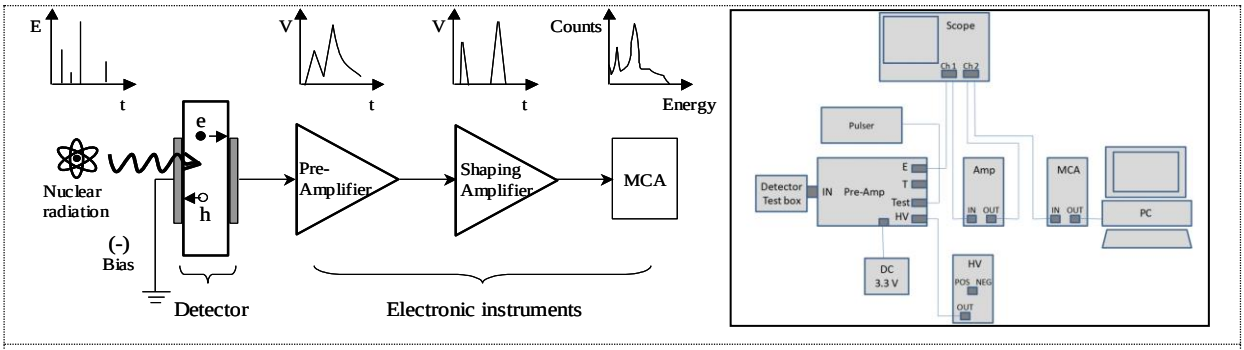

Figure 42. Schematic of detection testing setup.

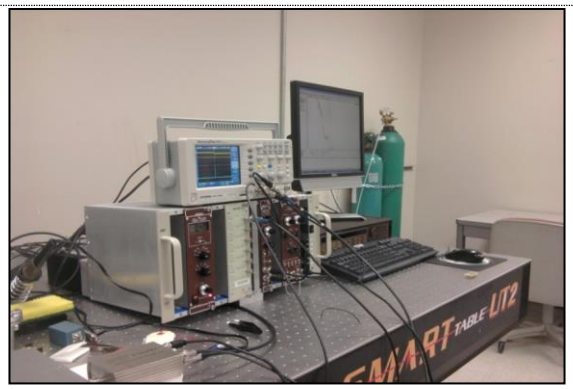

Figure 43. Detector Characterization Set-up

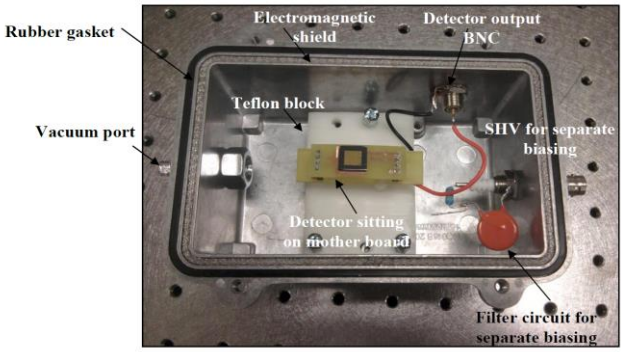

Figure 44. Detector testing stage

Initially, the detector responses were recorded without a source. The response of the detector was tested using an ^{241}Am source as described above. The response for gamma particles was measured by blocking the alpha particles using a piece of paper. The spectra were acquired at room temperature of 300K. Figure 45 shows the response of the detector for alpha and gamma particles. By comparing responses for γ and $\alpha + \gamma$ from Figure 45, it is clear that the detector shows distinct signal when it is radiated by alpha particles. Because the channel number is proportional to the energy of particles, it can be stated that the counts for $\alpha + \gamma$ particles are from high energy particles. This result clearly shows that the a-Se (B, As, Cl) detector can detect neutrons.

Figure 46 compares detector performance between devices without electron blocking layer and with Al/Al_2O_3 electron blocking layer. From Figure 46 (a) and (b), it is clear that the detector with electron blocking layer shows a higher signal to noise ratio by comparing counts between no source and with ^{241}Am source. Detectors with hole blocking layer Au/Sb_2S_3 did not improve the detection performance significantly. It is probably due to the fact that the antimony sulfide layer deposition is not optimized as we discussed above.

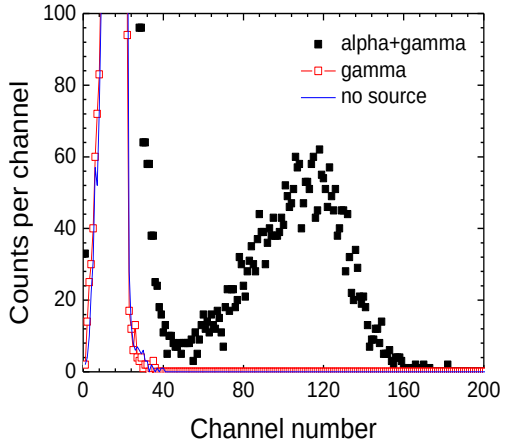

Figure 45. B-doped Se alloy detector test using ^{241}Am source. (Bias: -1000V, Coarse gain: 30, Fine gain: 3-00, Shaping time: 2 μs, Acquisition time: 120 s)

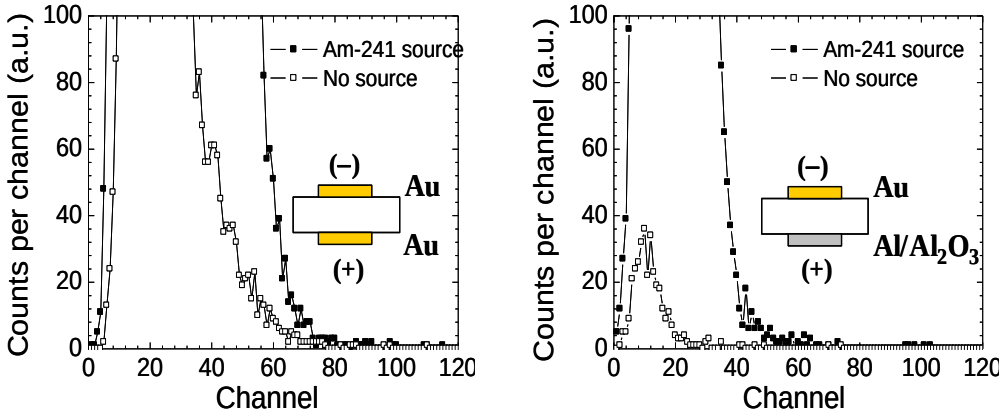

(a) (b)

Figure 46. B-doped Se alloy detector response comparison. (a) Without electron blocking layer (b) With electron blocking layer (Bias: -1000V, Coarse gain: 30, Fine gain: 3-00, Shaping time: 0.5 us, Acquisition time: 60s)

After screening procedures described above, we tested detectors with 0.7 μCi ^{252}Cf and 1Ci Pu-Be neutron sources. Figure 47 shows the detection testing systems. Figure 48 shows the detection spectrum of B-doped Se alloy detector with electron blocking layer under 0.7 μCi ^{252}Cf source. The spectrum shows two characteristic peaks of thermal neutrons via ^{10}B (n, alpha) reaction with the peak ratio of 8.4:1, which is lower than that of the theoretically predicted spectrum. Nevertheless, this result shows that the B-doped Se alloy detector can detect thermal neutrons. Figure 49 shows the detection spectrum of a B-doped Se alloy detector for 1 Ci Pu-Be source. By comparing the spectra with and without the Pu-Be source, it is clear that the large numbers of counts are generated by Pu-Be source.

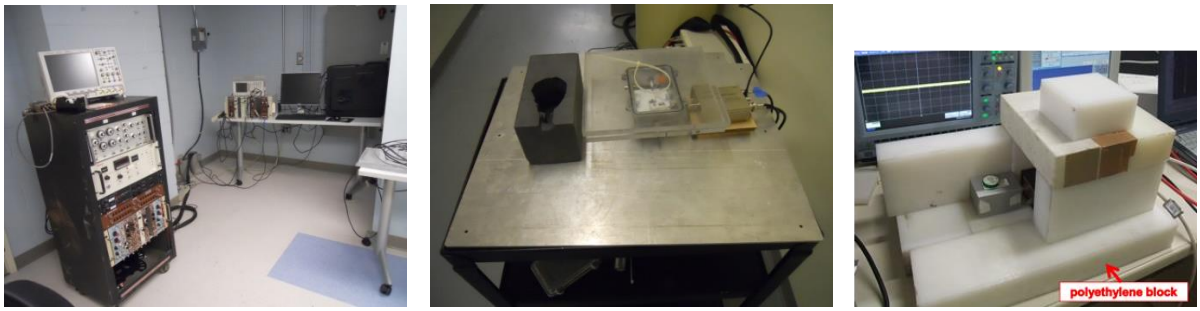

Figure 47. (Left) Detection system is situated outside of the neutron source vault chamber; (middle) detector electronics and sample box is within the neutron vault chamber and are sandwiched between 4-12 sheets of 0.5" thick acrylic; (right) Detector electronics are placed within a stack of high-density polyethylene (HDPE) moderator during measurements.

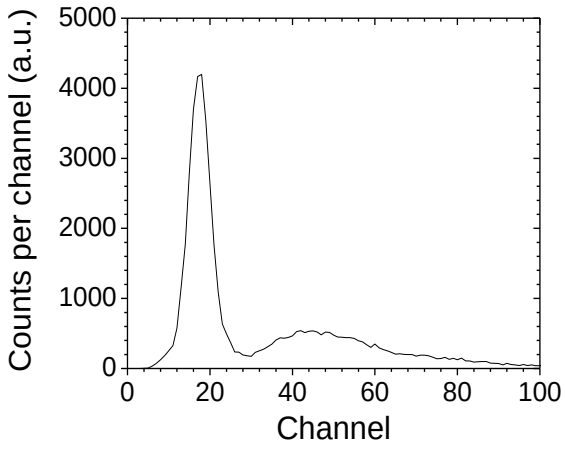

Figure 48. B-doped Se alloy detector test using ^{252}Cf source. (Bias: -1000V, Coarse gain: 30, Fine gain: 4-00, Shaping time: 1 µs, Acquisition time: 120 s)

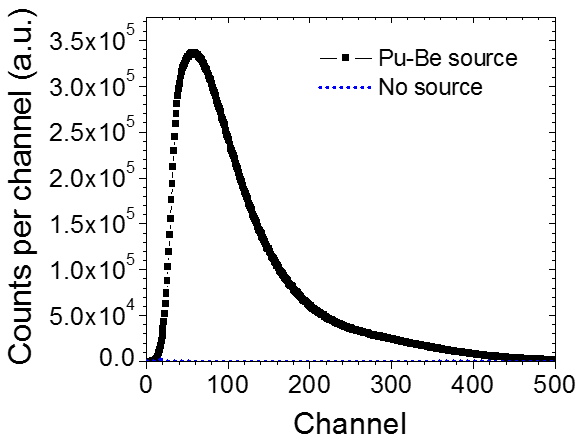

Figure 49. B-doped Se alloy detector test using Pu-Be source. (Bias: -1000V, Coarse gain: 30, Fine gain: 4-00, Shaping time: 1 µs, Acquisition time: 120 s)

In order to investigate the detector characteristics thoroughly, filters such as high density polyethylene (HDPE, ~ 1 inch thick) materials was used to thermalize the fast neutrons. For the testing with filters, we have designed and fabricated a setup as shown in the Figure 53. The source is put on the top of the setup where guide pins are located to ensure the same source location for every testing. The filters was added on the middle plate where a square hole is cut to allow nuclear particles to pass through and reach to a detector at the bottom of a Faraday cage. During testing, the Faraday cage is closed to reduce electromagnetic noise. Using this setup and filters, the B-doped and Li-doped a-Se alloy detectors were tested again with ^{252}Cf source. By comparing spectra of no filter with that of a HDPE filter, we can see counts due to fast neutrons and thermal neutrons.

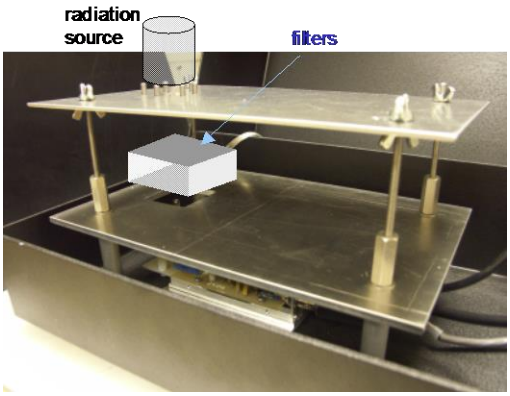

Figure 50. Designed and fabricated experimental setup to use for testing detectors with filters. (The radiation source and filters are drawn for guide.)

Detection Spectra of B-doped a-Se alloy detector under 0.7 μCi ^{252}Cf source with a stack of four 0.25″ high-density polyethylene (HDPE) moderator placed ~3cm from the source are shown in Figure 51. No peak was observed for the spectra taken without any source (black flat line seen in the figure on left) and characteristic peak of thermal neutron detection was observed for the spectra taken with ^{252}Cf source and HDPE moderator. With varying detector bias voltages (varied from 200 – 800V) peak was shifted and resolution was slightly reduced at higher voltage (>400V). The experiments were also carried out at varying acquisition time. For example, in Figure 51, the spectra on left were taken using 120 sec acquisition time and the spectra on right were taken using 60 sec acquisition time. Resolution was better with higher acquisition time. Therefore, subsequent detector testing were carried using 120 sec acquisition time.

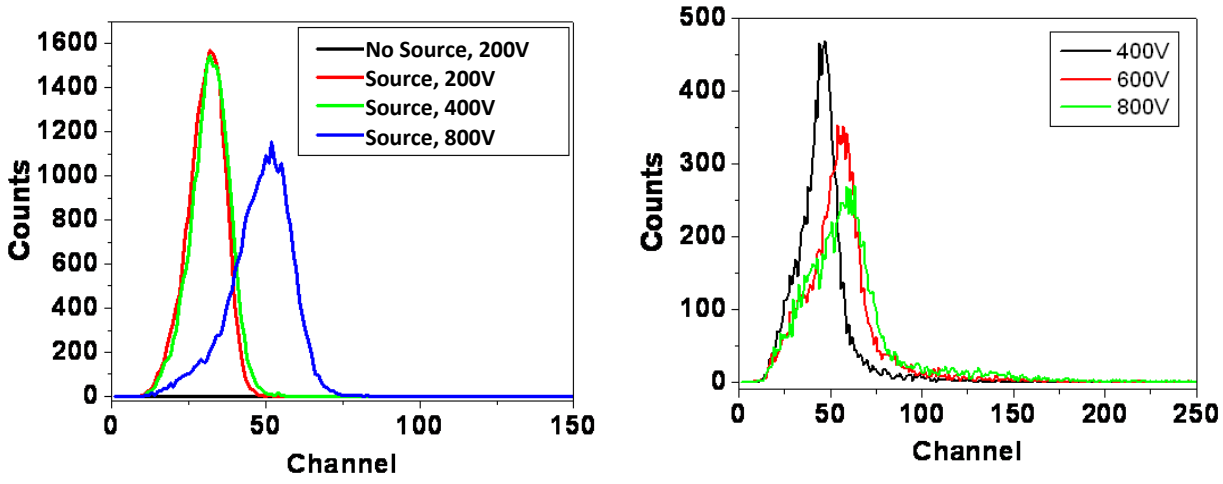

Figure 51 Detection spectra of B-doped a-Se-alloy detector under 0.7 μCi ^{252}Cf source at different bias voltages. The peak shifted with voltages as expected. A stack of four 0.25" high-density polyethylene (HDPE) moderator was used; (gain 3, 0.5 μs). Acquisition time was varied: (left) 120 sec and (right) 60 sec.

With 0.7 μCi ^{252}Cf source and a stack of four 0.25 inches of high density polyethylene (HDPE) moderator, detectors were tested with various gains and shaping time settings to optimize resolution. For this experiments, the detector was biased at 400 V and acquisition time was set at 120 sec. The results for ^{6}Li-Se detectors are shown in Figure 52 (spectra in the left). As can be seen from the spectra, the shorter shaping time provides a sharper peak with higher resolution. Using the gain at 3 and shaping time at 0.5 μs, which have been identified as the best in above experiments, Li-Se detectors were further tested at different bias voltages with an acquisition time of 120 sec. The results are also shown in Figure 52 (spectra in the right). The peak shifted with voltages as expected.

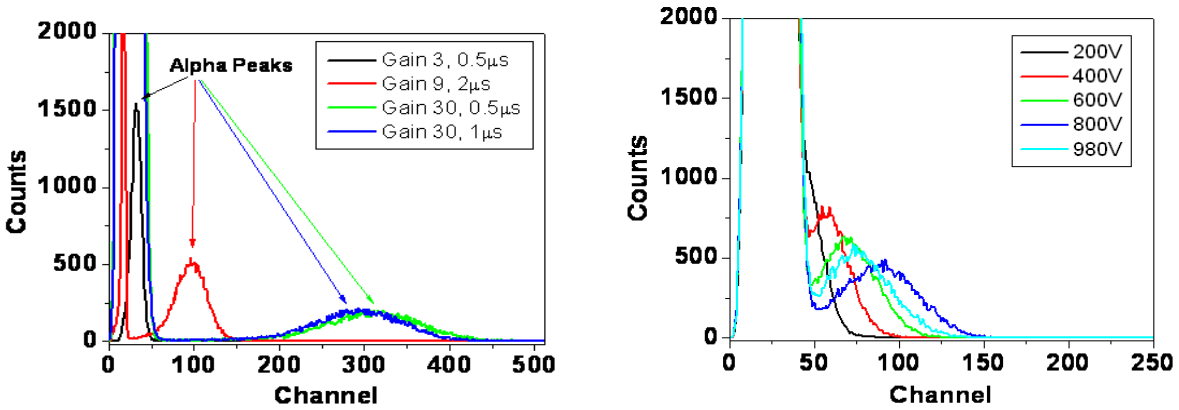

Figure 52. Detection spectra of Li–doped Se-alloy detector under 0.7 μCi ^{252}Cf source: (left) spectra for detector biased at 400 V and with various gains and shaping times; (right) spectra with different bias voltages and with gain at 3 and shaping time at 0.5 μs. Acquisition time was set at 120 sec and a stack of four 0.25" high-density polyethylene (HDPE) moderator was used for these testing.

6. Underachieved Milestone

We could not attain very high quality, high resistive, large area films (10×10 cm^2) boron- or lithium-doped a-Se (B, As, Cl)] alloy films with > 500 μm thickness and with B or Li doping concentration of 38 a/o (atomic percentage). As film thickness approaching to ≥500 μm, large area films (10 × 10 cm^2) showed induced polycrystallinity and inclusions/precipitates with low resistivity (cf. Figure 22). Thicker films preparation involved longer hours (≥ 10 hours) taking into consideration full pumping-up, baking interior fixtures, substrate heating & stabilizing, and final pumping-down with slow cooling rate. Therefore in films with a thickness of > 500 μm, it was difficult to preserve complete amorphous structure during long run time because of induced strain with higher thickness caused by induced crystallization (poly-crystallinity). We have tried to increase boron concentration in a-Se (B, As, Cl)] bulk alloy materials to 38 a/o. However we have faced difficulties with boron segregation within mono-dispersed alloy materials (Figure 53 and Figure 54). This may be due to inherent solid solubility of boron within the alloy liquid melt.

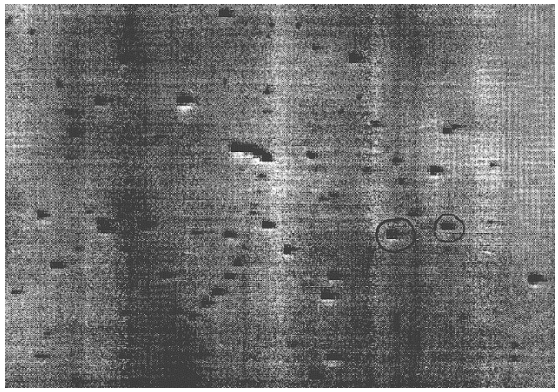

Figure 53. Induced crystallization observed with higher boron concentration due to inherent solid solubility of boron within B-Se alloy liquid melt; film thickness 450 μm and boron concentration 38 a/o (atomic percent).

Electron beam induced current (EBIC) imaging and IR transmission was used for further investigation of thicker films (>480 μm) with higher doping concentration (B or Li at > 32 a/o). The EBIC measurements were performed at room temperature (RT) under dark conditions using JEOL-35 SEM. The reverse bias of 175 V was applied to the detector for obtaining the EBIC contrast. IR transmission and EBIC images of ^{6}Li-Se (As, Cl) alloy detector shows non-uniform distribution of ^{6}Li inclusions/precipitates in a-Se (As, Cl) alloy. The IR image of the ^{6}Li-Se (As, Cl) alloy detector is shown in Figure 54(a), where the black spots indicate a few ^{6}Li inclusions/precipitates. The dark gray regions represent ^{6}Li-rich regions where ^{6}Li is segregating into inclusions, and light gray area represents stoichiometric ^{6}Li-Se (As, Cl) alloy material. The EBIC image of the reverse biased ^{6}Li-Se (As, Cl) alloy detector shown in Figure 54(b) consists of interpenetrating dark and white regions corresponding to high and low value of EBIC current respectively. This EBIC contrasts corresponds to non-uniform distribution of ^{6}Li confirming presence of large clusters of point defects which are believed to be the predecessor of ^{6}Li inclusions/precipitates shown in the IR image. These crystallographic defects often introduce deep energy levels into the band gap and therefore act as effective recombination centers. Therefore minority carrier lifetime in the defective region is lower than that in the defect-free region. Therefore the total collected current in the defective region is lower than that in the defect-free region. However, the leakage current through the detector might be significant under electron irradiation (EBIC signal) and under high bias voltage applied during EBIC measurements. This leakage current is higher in the defective regions. Therefore dark regions in Figure 54(b) correspond to clusters of point defects having high leakage current, whereas white regions represent areas devoid of any point defect clusters.

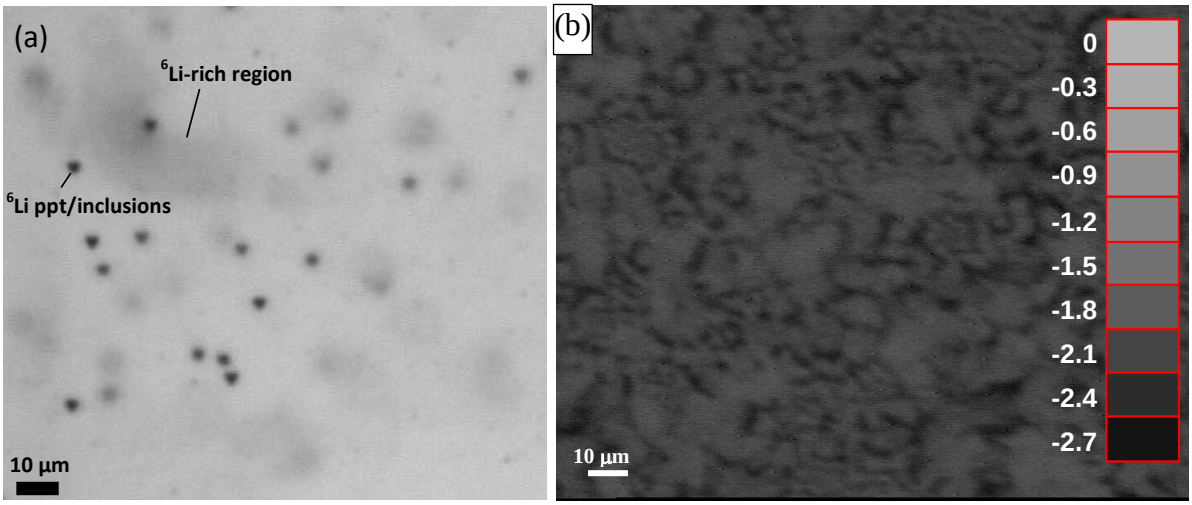

Figure 54. (a) A typical IR transmission image of ^{6}Li-Se (As, Cl) alloy detector and (b) EBIC image of the same ^{6}Li-Se (As, Cl) alloy detector at 175 V reverse bias.

7. Student Training

Six graduate students and one postdoctoral fellow worked on this project.

1) Mr. Khai Nguyen who has worked on calibration, noise analysis, and nuclear testing completed his MS, and will complete his Ph.D. by December 2017. He has recently joined as an Electrical Engineer, Imaging, Robotics, and Radiation Systems, R&D Engineering, Savannah Research National Laboratory, SC 29808.

2) Dr. Rahmi O. Pak, who worked on thin film preparation, characterization, and device testing, has completed his Ph.D. in May 2017 and has now joined as a Research Engineer at Argonne National Laboratory, IL 60439.

3) Dr. Mohammad A. Mannan, who partly worked on the purification, alloy synthesis, and material characterization of a-Se alloys and films, has completed his Ph.D. degree in 2015 and joined as a Process Technology Development Engineer at Intel Corp., 2501 NW 229th Ave, Hillsboro, OR 97124.

4) Dr. Sandip Das, who worked on the synthesis and characterization of a-Se alloy materials for radiation detectors, has completed his Ph.D. degree in 2014 and is now a tenure track Assistant Professor at Kennesaw State University, Marietta, GA 30060.

5) Mr. Abhinav Mehta, who worked in this project as a graduate student, has completed his M.S. thesis entitled "High Resistivity Amorphous Selenium Alloy Semiconductors for Radiation Detection Applications" in July 2013 and joined as a Program Analyst in ERPA Analysis Group, Inc.

6) Mr. Chian Oner, who has mostly worked on lithium-doped a-Se alloy detectors is now working on his dissertation and he will graduate in May 2018.

7) Dr. Sandeep K. Chaudhuri worked on this project as a Post-Doctoral Fellow and joined as an UGC Assistant Professor of the Center for Applied Physics, Central University of Jharkhand, Brambe, Ranchi 835205, India.

8. List of Publications

1. Krishna C. Mandal, Enriched Boron-Doped Amorphous Selenium Based Position Sensitive Solid-State Thermal Neutron Detector, Presented at the MPACT/MRWFD Working Group Meeting, Marriott Albuquerque Uptown, Albuquerque, NM, March 28-31, 2017.
2. C. Oner, and T. A. Chowdhury, R. O. Pak, and K. C. Mandal, "Thermally Evaporated B- and Li-Doped Amorphous Selenium Alloy Based Radiation Detectors," Abstract # 2664, Presented at the 2016 IEEE Medical Imaging Conference, Nuclear Science Symposium, and 23rd International Symposium on Room Temperature Semiconductor X- and Gamma-ray Detectors, Oct. 29 – Nov. 06, Strasbourg, France, To be submitted to IEEE Trans. On Nuclear Science, 2017.
3. Towhid A. Chowdhury, Cihan Oner, and Krishna C. Mandal, "Amorphous Selenium (a-Se) Alloy Detectors for X-rays and High Energy Nuclear Radiation Detection," 2016 IEEE Nuclear Science Symposium & Medical Imaging Conference, and the 23rd International Symposium on Room-Temperature Semiconductor X-ray and Gamma-ray Detectors, Oct. 29 – November 05, Strasbourg, France, IEEE Conf. Record, RO9-55, 5 pages, 2017.
4. Krishna C. Mandal, Sandeep K. Chaudhuri, Khai Nguyen, Rahmi Pak, M. A. Mannan, Arnold Burger, and Michael Groza, "Solid-State Thermal Neutron Detectors Based on Enriched Boron-Doped Amorphous Selenium," Featured talk presented at the Fuel Cycle Technologies Annual Meeting, Idaho National Laboratory, November 4-6, 2014.
5. Cihan Oner, Towhid A. Chowdhury, Rahmi O. Pak, and Krishna C. Mandal, "Studies of low leakage current radiation detectors on thermally evaporated B- and Li-doped amorphous selenium alloy films," Paper # 9968-53, Presented at the SPIE Optics+Photonics, Hard X-ray, Gamma-Ray, and Neutron Detector Physics XVIII, August 28 – September 1, 2016, San Diego, CA, USA.
6. Krishna C. Mandal, Cihan Oner, Rahmi O. Pak, and Towhid A. Chowdhury, "Studies of Radiation Detection Properties and Leakage Currents on B- and Li-Doped Amorphous Selenium Alloy Films," Presented at the 7th International Conference on Optical, Optoelectronic and Photonic Materials and Applications (ICOOPMA2016), Montréal, Canada, June 12 - June 17, 2016, To be submitted to Journal of Materials Science: Materials in Electronics (Springer), 2017.
7. Cihan Oner, Khai V. Nguyen, Rahmi O. Pak, Towhid Chowdhury, and Krishna C. Mandal, "Investigation of Metal Contacts on High-Resistivity Large-Area Amorphous Selenium Alloy Films," IEEE 2015 Medical Imaging Conference, Nuclear Science Symposium (NSS) and Symposium on Room-Temperature Semiconductor X-ray and Gamma-Ray Detectors (RTSD), Oct. 31–Nov. 07, San Diego, California, IEEE Conf. Record, R3A-41, 6 pages, 2015.
8. Cihan Oner, Khai V. Nguyen, Rahmi O. Pak, Mohammad A. Mannan, and Krishna C. Mandal, "Investigation of thermally evaporated high resistive B-doped amorphous selenium alloy films and metal contact studies," Presented at the 2015 Optics+Photonics, SPIE Conf. #9593, Hard

X-Ray, Gamma-Ray, and Neutron Detector Physics XVII, San Diego, Aug. 10 – 12, 2015, SPIE Proc., 9593, 95931I-1-11, 2015.

9. R. O. Pak, K. V. Nguyen, M. A. Mannan, S. K. Chaudhuri, and K. C. Mandal, "Amorphous Selenium Stabilized Alloys for Nuclear Radiation Detector Applications," IEEE Nuclear Science Symposium (NSS), Medical Imaging Conference (MIC), and 21st Symposium on Room-Temperature Semiconductor X-ray and Gamma-Ray Detectors (RTSD), November 08 – November 15, Washington State Convention Center, Seattle, WA, USA.
10. Abhinav Mehta, Sandeep K. Chaudhuri, Yunlong Cui, Michael Groza, Arnold Burger, Krishna C. Mandal, "Characterization of amorphous selenium alloy detectors for x-rays and high-energy nuclear radiation detection," Presented at the 2013 Optics+Photonics, SPIE Conf. #8852, Hard X-Ray, Gamma-Ray, and Neutron Detector Physics XV, San Diego, Aug. 25 – 29, 2013, SPIE Proc. Vol. 8852, 88521O-1-7, 2013.
11. Ramesh M. Krishna, Sandeep K. Chaudhuri, Peter G. Muzykov, and Krishna, C. Mandal, "Synthesis and Characterization of Amorphous Selenium Alloys for Radiation Detector Applications," Presented at the 2012 SPIE Optics+Photonics conference, San Diego, CA, August 12-16, 2012, Abstract #8507-25.
12. Sandeep K. Chaudhuri, Abhinav Meheta, Yung Long Cui, Michael Groza, Arnold Burger, and Krishna, C. Mandal, "Preparation and Characterization of Amorphous Selenium Stabilized Alloys for Nuclear Radiation Detectors," Presented in the Materials Research Society Meeting in San Francisco, CA, 2013.